J. Fluid Mech. (2012), *vol.* 697, *pp.* 1–34. © Cambridge University Press 2012
doi:10.1017/jfm.2012.1

Modelling lateral manoeuvres in fish

K. Singh†‡ and T. J. Pedley

Department of Applied Mathematics and Theoretical Physics, University of Cambridge, Wilberforce Road, Cambridge CB3 0WA, UK

(Received 14 March 2010; revised 26 October 2011; accepted 2 January 2012; first published online 7 March 2012)

We propose a method to model manoeuvres in self-propelled flexible-bodied fish by modelling the hydrodynamics coupled to the body inertia. Flexible body motion is prescribed and the equations of motion are solved for the position of the centre of mass and rotation of the body. The governing equations are formulated by applying the conservation of linear and angular momentum. Two independent methods to model the fluid dynamics are pursued: Model 1 is an extension of elongated-body theory, modified for self-propulsion and flexible motion. Model 2 applies a numerical boundary-element formulation with the fish modelled as an infinitely thin rectangular body. The manoeuvring response to an impulsive input is first examined to understand the rigid-body characteristics of the fish. A flexible bend action is included to model C-bends of the type observed during escapes in fish. Models 1 and 2 are used to cross-verify the respective implementations as well as to develop physical insights into manoeuvring. A parameter study shows that fish of intermediate body depths are best adapted to rapid turns whereas the initial dynamic state of the fish is instrumental in affecting the sign as well as the magnitude of the turn angle, for a prescribed bend deflection. Computations for combined swimming and turning show that the initial rigid-body dynamics of the fish is much more effective than the induced effect of the prior shed wake in enhancing the turning response.

Key words: swimming/flying, vortex interactions, vortex shedding

1. Introduction

The objective of this work is to develop a three-dimensional model of a self-propelled fish capable of flexible time-varying asymmetric deflections. The motivation is to understand the mechanics of locomotion that a fish would typically perform. It is interesting that theoretical work on the fluid dynamics of fish locomotion has almost exclusively focused on the problem of forward propulsion, with some noteworthy exceptions (Weihs 1972; Kambe 1978). However, one might argue that the sheer number and variety of adaptations in fish species cannot be explained merely by the need to evolve to the fastest or the most efficient swimming stroke. Environmental factors such as habitat and predators are likely to contribute to variation in fish morphology and adaptations (such as fins) that could affect the ability of fish species to survive or be driven to extinction. Living organisms are affected by their

† Email address for correspondence: kiran.singh@cantab.net
‡ Present address: OCCAM, Mathematical Institute, 24-29 St Giles, Oxford OX1 3LB, UK.

https://doi.org/10.1017/jfm.2012.1 Published online by Cambridge University Press

environment and mechanisms of locomotion in animals should evolve accordingly. In order to understand these aspects, a general model of flexible motion is needed.

The principal focus of this work is to understand the coupling between inertia and hydrodynamics of self-propelled fish in flexible manoeuvres. Body inertia of the fish intrinsically affects its response and must be included when developing the governing equations. We build upon the large-amplitude undulatory swimming model developed by Hill (1998), who developed a numerical boundary-element method to model an infinitely thin rectangular fish of finite aspect ratio. In this work we concentrate on more general locomotion: thus we extend the approach to model manoeuvres, although still in rectangular-shaped bodies. For verification of the numerical model and for optimisation purposes, the work of Kambe (1978) is extended to model flexible turns.

The body length, l, of the fish forms the principal length scale which is used to define the Reynolds number $Re = Ul/\nu$ of the flow, where ν is the kinematic viscosity of water and U is the characteristic swimming speed. In the literature, swimming speeds in fish are invariably defined in body lengths travelled per second. Thus Re scales as l^2 and it is easy to classify swimmers, based purely on their length, into $Re \ll 1$ swimmers, for which the fluid inertia is negligible compared to the viscosity, and $Re \gg 1$ swimmers for which the viscous contribution is significantly less important than the fluid inertia. In this study we restrict ourselves to the $Re \gg 1$ swimming range.

Although the goal of this work is to model and understand flexible-body manoeuvres, theoretical analysis and experimental research on forward propulsion has progressed a great deal further than work on manoeuvring, and so we use the body of knowledge on undulatory swimming as a point of departure. From a mathematical modelling perspective the classical theories on fish swimming are those of Lighthill (1960) and Wu (1961). Lighthill used slender-body theory to model fish where the cross-wise dimension is much smaller than the length, the cross-sectional area varies slowly along the length, and the fish propels itself forward by generating small-amplitude lateral undulations. A key conclusion of Lighthill's theory was that the propulsive efficiency of the fish could be maximised by generating lateral deflections that are rearward travelling waves of increasing amplitude along the body length, with a wave speed that is around 5/4 times that of the steady swimming speed. He showed that the typical fish body shape was optimal to minimise sideways oscillatory motion or lateral recoil. The theory, sometimes referred to as Lighthill's reactive force theory, was extended by Lighthill (1971) to model large-amplitude flexible swimming. It has been applied extensively in the literature to understand and interpret hydrodynamic differences between species of fish (see for instance Weihs 1972; Videler & Hess 1984).

Despite the advantages of the elegant slender-body theory, the main problem is that it neglects the wake shed at the trailing edge or tail of the fish, which in turn affects the upstream fluid velocity and the pressure difference across the body. This is not a problem in the waving plate theory proposed by Wu (1961), which was developed as a model of the hydrodynamics of a flexible swimmer in two dimensions. Complex variable theory was used to model the infinitely thin swimmer performing undulatory motion defined by progressive waves of prescribed wavelength and phase travelling down the body length, akin to the approach developed in Lighthill (1960). Unlike Lighthill's theory however, Wu's formulation is two-dimensional and might be interpreted as representative of the flow field in the plane of symmetry of the swimmer, where three-dimensional effects are the least significant. The two theories, of Lighthill (1960) and Wu (1961), form the cornerstone of the analytical formulation

https://doi.org/10.1017/jfm.2012.1 Published online by Cambridge University Press

of high-*Re* undulatory swimming and although they have been improved upon and enhanced in their application, the essential theories remain extremely insightful. In work not presented here, we used Wu's approach to verify the numerical boundary element method (Model 2) in the limits of infinite depth (Singh 2009). A recent review by Wu (2011) includes a comprehensive summary of these theories and subsequent works that relate to various aspects of fish swimming.

When viscous effects are included, the resistive force theory of Taylor (1952) has been successfully applied. Such a model has been used recently by McMillen & Holmes (2006) and McMillen, Williams & Holmes (2008) to model swimming in lamprey. In Taylor's model the assumption is that the instantaneous flow due to relative motion between the body and the fluid can be treated as quasi-steady. Although such a model is valid for low-*Re* flows the errors associated with neglecting the unsteady added mass become significant as fluid inertia becomes more important. A good compromise is the combined resistive–reactive force theory of Lighthill (1977) that includes the longitudinal effects of flow separation with the unsteady undulatory mode of swimming. Kambe (1978) employs a similar approach in his analysis of impulsive turns by a carangiform fish, modelled as a tail-less rigid elliptical body. This work combines the Lighthill (1960) elongated-body theory with a correction for wake shedding (Wu 1971*b*); it also includes the resistive-force theory of Taylor (1952) to model viscous drag. To implement the model of a turn, asymmetric lateral action was represented as an impulsive force at the tail and the direction of motion in response to such a forcing was calculated. The role of body inertia and geometry parameters was then examined. In Model 1, we extend Kambe's approach to model realistic fish manoeuvres effected by flexible-body deflections. The purpose of this model is two-fold: to develop physical insights into flexible-body manoeuvres and to validate the numerical model (Model 2).

Among the early experimental works on manoeuvres, the first sets of data on flexible-bodied turning in fish were made by Gray (1933). Through time-sequence photographs of various species, he was able to show the asymmetric body flexure leading to a change in orientation. It is now well-known that flexible swimmers generate forward propulsive thrust by means of laterally symmetric muscle contractions (Wu 1977). On the other hand, for manoeuvres to be effective these muscle contractions must be laterally asymmetric and of a finite time duration, over which time a change in orientation occurs. Weihs (1972) analysed Gray's turning data for goldfish (*Cyprinus auratus*) and rudd (*Cyprinus erythropthalmus*), to consider the mechanics of turning. Weihs split the body into three discrete entities and the turn into three stages, and the contributions of the anterior, mid and posterior parts during each stage were analysed. McCutchen (1976) used the shadowgraph technique to experimentally visualise the fluid response in the vicinity of the Zebra danio (*Brachydanio rerio*) during a turn. Two distinct vortex wakes were shed by the swimmer. A small wake was seen initially, on the side corresponding to the turn. At the end of the turn a large vortex wake was observed to be shed, oriented in the new direction of swimming. Kambe (1978) conjectured that the vortex rings in the wake impart a reactive force to the body and may thereby assist in turning. More recently Wolfgang *et al.* (1999) used the particle image velocimetry (PIV) technique to visualise the vortex wake generated by a turning giant danio (*danio malabaricus*) and employed their numerical model to observe vortex formation during a prescribed turn. In this work we use the numerical model of the self-propelled fish to investigate the role of vortex wake interactions in enhancing manoeuvrability.

https://doi.org/10.1017/jfm.2012.1 Published online by Cambridge University Press

Kanso (2009) applied the theory of Lighthill (1960) to model self-propulsion by a fish due to prescribed body shape functions, the position of the fish in space being determined by applying momentum conservation between the shed wake and the unsteady reactive forces. By neglecting body inertia and other body forces, the problem is exclusively one that balances the unsteady inviscid fluid and viscous fluid components. This approach, perhaps valid for propulsive swimming, becomes less applicable for manoeuvres where the inertia of the body cannot be neglected. A self-propelled swimming model of a fish that includes body inertia has been recently developed by Boyer, Porez & Leroyer (2010) to model the three-dimensional motion of an eel-like fish. They used the large-amplitude theory of Lighthill (1971) coupled with the resistive force theory of Taylor (1952) to model the viscous drag and in Boyer *et al.* (2008) they show good agreement with the three-dimensional Navier–Stokes solutions for an eel-like ellipse-shaped fish. This work thus serves as independent validation of Lighthill's theory.

In this work we focus on the self-propelled motion of a fish in an inviscid fluid that includes the wake shedding at the tail. The fluid models considered are the elongated-body theory adapted for wake shedding by Wu (1971*b*) and a numerical boundary-element method with the Kutta condition applied at the tail (as implemented by Hill 1998). Based on prior experimental and theoretical work, we note that the unsteady motion of a self-propelled fish depends upon several factors, including: the lateral deflection function, initial conditions, body inertia and body dimensions. In this paper we investigate these factors from the perspective of the role they play in fish manoeuvrability. In § 2, we present the kinematic formulation and develop the equations to model rigid-body motion and flexible motion explicitly. The equations of motion for planar motion are formulated using the conservation of linear and angular momentum. In § 3 we examine the two fluid-dynamic models used in this work. Model 1 is the flexible-body extension to the analytical formulation used by Kambe (1978), Model 2 develops the three-dimensional numerical boundary-element formulation for a rectangular-shaped fish in an inviscid fluid. The models are verified and used to examine aspects related to rigid and flexible manoeuvres in § 4. Based on observations (Gray 1933), a test deflection function is proposed and applied to analyse the turning response to a lateral bend. In § 5 we use these models to find an optimal body depth from a manoeuvrability perspective. We then use the optimal configuration to examine the role of different initial conditions and the prior shed wake in enhancing the turning response of a self-propelled fish.

2. Flexible manoeuvres: formulating the equations of motion

In this section we consider the model used to represent the fish as it swims in a quiescent fluid. Curve $\mathscr{C}(s,t)$, in the sketch in figure 1, represents the fish, parameterised by the Lagrangian coordinate s and time t. The laboratory frame of reference, $\{\hat{\boldsymbol{i}}, \hat{\boldsymbol{j}}, \hat{\boldsymbol{k}}\}$, is fixed in space at point O and the body frame, $\{\boldsymbol{e}_x, \boldsymbol{e}_y, \boldsymbol{e}_z\}$, is fixed on the centre of mass of the fish (referred to as point P in the sketch). P' is a reference point on the body a Lagrangian distance, s_o, from the nose with respect to which the flexible-body deflections are defined. P' is defined so that when the fish centre-line is straight, P and P' coincide; $\boldsymbol{e}_x$ is tangent to the body at P' making an angle θ with $\hat{\boldsymbol{i}}$. Although the fluid-dynamic model is three-dimensional, the fish motion is confined to the two-dimensional plane, $\{\boldsymbol{e}_x, \boldsymbol{e}_y\}$ (equivalently, $\{\hat{\boldsymbol{i}}, \hat{\boldsymbol{j}}\}$; this equivalence holds as $\boldsymbol{e}_z$ is parallel to $\hat{\boldsymbol{k}}$).

https://doi.org/10.1017/jfm.2012.1 Published online by Cambridge University Press

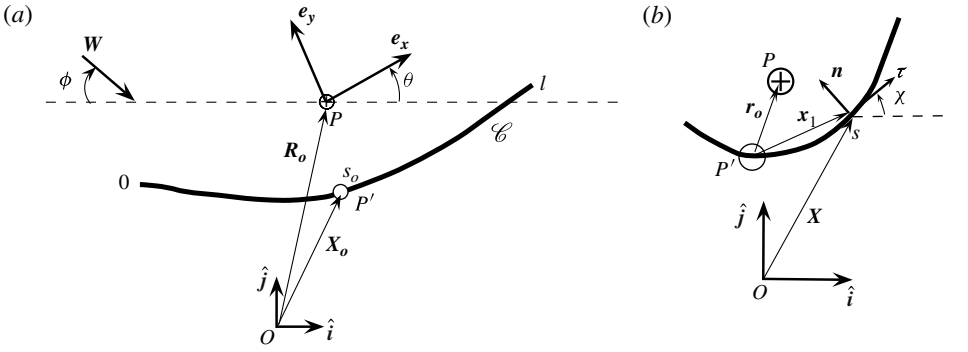


FIGURE 1. (*a*) The mid-line of the flexible swimmer is represented by curve $\mathscr{C}$, parameterised by the Lagrangian coordinate s and time t. The body moves with speed, $-\boldsymbol{W}(t)$, relative to the fluid. $\theta(t)$ is the tangent angle made by the body at P', the reference point on $\mathscr{C}$ at a Lagrangian distance s_o from the nose. The body frame of reference $\{\boldsymbol{e_x}(t), \boldsymbol{e_y}(t)\}$ is defined at the fish centre of mass, P, at position vector $\boldsymbol{R}_o(t)$ with respect to the fixed origin, O. (*b*) A close-up view near P and P' indicates the prescribed deflection, $\boldsymbol{x}_1(s, t)$, of a point s on the curve defined with respect to P', and with position vector $\boldsymbol{X}(s, t)$. At s the local tangential basis, $\{\boldsymbol{\tau}(s, t), \boldsymbol{n}(s, t)\}$, makes an angle $\chi(s, t)$ with the fixed basis.

We assume the fish is initially gliding with speed, U, oriented along $-\hat{\boldsymbol{i}}$ (which means that at the start of the computation $\boldsymbol{e_x}$ is coincident with $\hat{\boldsymbol{i}}$). In order to generate any kind of motion such as a turn, the fish contracts its muscles which leads to observed body deflection, $y(s, t)$. In our model, the local flow around the fish is perturbed such that the velocity of the fluid particles, $\boldsymbol{v}$, tends to zero as the distance from the body increases. We solve the equations of motion to determine the response of the fish to the inviscid forces generated due to the local perturbed flow and the inertial reaction of the fish. The response of the fish can be characterised by the orientation of the body frame, $\theta = \cos^{-1}(\boldsymbol{e_x} \cdot \hat{\boldsymbol{i}})$ and the velocity vector of the centre of mass, $\boldsymbol{V}_o(t)$ (equivalently the relative velocity of the fluid, $\boldsymbol{W} = -\boldsymbol{V}_o$). Solutions are obtained depending upon the initial conditions and the prescribed flexible-body deflection, $y(s, t)$. In § 2.2 we define the kinematics for the fish: first the rigid-body kinematics is described, then we introduce the generalisation for flexible-body locomotion. The equations of motion are derived in § 2.3.

2.1. *Dimensional scaling*

In the numerical representation, the fish is modelled as a flexible, infinitely thin, rectangular plate of dimensional length $\bar{l}$ and principal depth dimension, $\bar{d}$. The dimensional parameters used to non-dimensionalise the equations are therefore the body length, $\bar{l}$, initial swimming speed $\bar{U}$ and fluid density $\bar{\rho}$ (dimensional variables are distinguished by an overbar). The body is considered inextensible and we define coordinate s as the distance of a Lagrangian point along the body axis, varying from 0 at the nose to $\bar{l}$ at the tail.

The configuration of the swimmer is such that, initially, it is stretched straight and coasting along $-\hat{\boldsymbol{i}}$ at speed $\bar{U}$. Consider the scenario where we model an asymmetric turn of the body, taking place over a time interval $\bar{t}_o$. The fish flexes its body into a C-shape after which it straightens out to resume coasting in a direction at an angle ϕ with $\hat{\boldsymbol{i}}$. The angle of the direction of motion, ϕ, is defined as distinct from the body

https://doi.org/10.1017/jfm.2012.1 Published online by Cambridge University Press

orientation, θ; these are only coincident if there is no side-slip. From measurements on goldfish and rudd (Gray 1933), a typical time scale $\bar{t}_o$ to perform a C-turn is of the order of one second (this is consistent with data on turns from Wu (1977)). In addition, during C-turns the swimmer moves at speeds of the order of a body length per second, thus for the bulk of the results we assume the non-dimensional time to manoeuvre is

$$t_o = \bar{t}_o \bar{U}/\bar{l} = O(1). \tag{2.1}$$

In order to specify the body mass distribution along the fish, we assume the fish has an elliptic body cross-section. However the longitudinal variation of mass distribution differs for the two models: in Model 2 we consider the simple case of uniform depth and therefore define a uniform mass per unit length. For Model 1, we generalise the formulation along the lines developed in Kambe (1978). This formalism models non-uniform depth and so we employ Model 1 to gain insights into the impact that variations in body geometry have on fish manoeuvrability. A general description of the body mass $\bar{M}_b$ can be defined for a fish that is assumed to be neutrally buoyant, with body density $\bar{\rho}_b = \bar{\rho}$, where $\bar{\rho}$ is the density of the fluid. The non-dimensional mass per unit length is given by

$$m_b(s) = \bar{m}_b(s)/(\bar{\rho}\bar{l}^2 d), \tag{2.2}$$

and

$$\bar{M}_b = \int_0^{\bar{l}} \bar{m}_b(s)\,\mathrm{d}s \tag{2.3}$$

is the total mass of the fish; $d = \bar{d}/\bar{l}$ is the ratio of maximum body depth to characteristic length. The Reynolds number $Re = \bar{l}\bar{U}/\bar{\nu}$, where $\bar{\nu}$ is the kinematic viscosity of the fluid, is typically of the order of 10^5–10^6 in adult fish.

2.2. *Kinematic description of the fish*

The complete motion of the body in the two-dimensional laboratory frame $\{\hat{\boldsymbol{i}}, \hat{\boldsymbol{j}}\}$ can be described as a linear combination of rigid-body motion (translation in $\{\hat{\boldsymbol{i}}, \hat{\boldsymbol{j}}\}$, rotation about $\hat{\boldsymbol{k}}$) and flexible motion (defined in the body frame, $\{\boldsymbol{e}_x, \boldsymbol{e}_y\}$). For purely rigid-body motion, the reference point on the body, P', coincides with the centre of mass of the fish, P. Let us first systematically develop the kinematics for the self-propelled swimmer, first for the rigid body (§ 2.2.1) and then for the flexible body (§ 2.2.2). (Note: position vectors referred to in upper case letters correspond to definitions in the inertial frame, defined with respect to the fixed origin, O; variables in lower case correspond to position vectors in the body frame.)

2.2.1. *Rigid-body motion*

The formulation in this section develops the kinematics of a freely moving, rigid, rectangular flat plate. We develop the system of equations and deduce the equations for the velocity vector of the rigid body, $\boldsymbol{V}_o(t)$, as well as the orientation, $\theta(t)$, from which we can ascertain the exact location and orientation of the plate in space, at every instant in time. $\boldsymbol{R}_o(t)$ is the position vector at time t of point P with respect to origin O. In addition, the body rotates through angle $\theta(t)$ about $\hat{\boldsymbol{k}}$. The body frame of reference is fixed at the centre of mass, P, of the fish and is given as

$$\boldsymbol{e}_x(t) = \cos\theta(t)\,\hat{\boldsymbol{i}} + \sin\theta(t)\,\hat{\boldsymbol{j}}, \tag{2.4}$$

$$\boldsymbol{e}_y(t) = -\sin\theta(t)\,\hat{\boldsymbol{i}} + \cos\theta(t)\,\hat{\boldsymbol{j}} \tag{2.5}$$

https://doi.org/10.1017/jfm.2012.1 Published online by Cambridge University Press

and the orientation angle, $\theta(t) = \tan^{-1}(\partial_s Y/\partial_s X)_{s=s_o}$, is the tangent angle at P' where X, Y are defined in (2.8). For a rigid body, curve $\mathscr{C}$ is a straight line that can rotate and translate in space and so $\theta(t)$ is the tangent angle to all points on the curve. Since the fish is allowed to move freely in space, the rigid body velocity (effectively the velocity of the centre of mass) is

$$\boldsymbol{V}_o(t) = V_{x_o}(t)\,\hat{\boldsymbol{i}} + V_{y_o}(t)\hat{\boldsymbol{j}}, \tag{2.6}$$

and its acceleration $\boldsymbol{A}_o(t) = \mathrm{d}\boldsymbol{V}_o/\,\mathrm{d}t$. The fluid velocity relative to the body is given as $\boldsymbol{W}(t) = -\boldsymbol{V}_o(t)$ and makes an angle ϕ with $\hat{\boldsymbol{i}}$ where $\phi(t) = \tan^{-1}(V_{y_o}/V_{x_o})$ is the direction of motion. The position vector of the centre of mass, with respect to the origin O, is

$$\boldsymbol{R}_o(t) = R_x(t)\,\hat{\boldsymbol{i}} + R_y(t)\,\hat{\boldsymbol{j}} = \int_0^t (V_{x_o}(t)\,\hat{\boldsymbol{i}} + V_{y_o}(t)\hat{\boldsymbol{j}})\,\mathrm{d}t. \tag{2.7}$$

The position vector of an arbitrary point s on $\mathscr{C}$ with respect to fixed point O is

$$\boldsymbol{X}(s,t) = X\hat{\boldsymbol{i}} + Y\hat{\boldsymbol{j}} = \boldsymbol{R}_o(t) + \boldsymbol{r}(s,t), \tag{2.8}$$

where $\boldsymbol{r}$, the position vector with respect to the centre of mass P, is defined in (2.10). With respect to figure 1 recall that P' and P are coincident on a rigid body.

2.2.2. *Kinematics of the combined flexible- and rigid-body motion*

Determining the instantaneous position of the centre of mass is non-trivial for flexible, self-propelled swimmers. We must distinguish between the reference point on the body, P', (at position vector $\boldsymbol{X}_o$, see figure 1), and the centre of mass, P (at $\boldsymbol{R}_o$). For a flexible body the centre of mass will shift as the body undergoes unsteady, flexible deflections; it will not in general lie on $\mathscr{C}$. Furthermore, the flexible motion is prescribed by defining the form of $\mathscr{C}$, so we need an independent reference point, P', at $s = s_o$ on $\mathscr{C}$. The position vector of P with respect to P' is

$$\boldsymbol{r}_o(t) = \frac{\displaystyle\int_0^l m_b(s)\boldsymbol{x}_1(s,t)\,\mathrm{d}s}{\displaystyle\int_0^l m_b(s)\,\mathrm{d}s}, \tag{2.9}$$

where $\boldsymbol{x}_1(s,t) = x_1(s,t)\boldsymbol{e}_x + y_1(s,t)\boldsymbol{e}_y$ is the vector distance of s defined with respect to P'. In our formulation $\boldsymbol{x}_1(s,t)$ is prescribed, and $\boldsymbol{r}_o(t)$ is determined so the position vector of point s defined with respect to the centre of mass is given as

$$\begin{aligned}\boldsymbol{r}(s,t) &= x(s,t)\boldsymbol{e}_x + y(s,t)\boldsymbol{e}_y \\ &= \boldsymbol{x}_1(s,t) - \boldsymbol{r}_o(t).\end{aligned} \tag{2.10}$$

We elaborate on the advantage of such a description later in this section. In this implementation, we prescribe $y_1(s,t)$ and enforce the length preserving criterion, which from (2.10) reduces to

$$x(s,t) = \int_0^s \left(1 - (\partial_s y(s,t))^2\right)^{1/2}\mathrm{d}s. \tag{2.11}$$

Note that the local tangential basis, $\{\boldsymbol{\tau}, \boldsymbol{n}\}$, at s is

$$\boldsymbol{\tau}(s,t) = \cos\chi\,\hat{\boldsymbol{i}} + \sin\chi\,\hat{\boldsymbol{j}}, \quad \boldsymbol{n}(s,t) = -\sin\chi\,\hat{\boldsymbol{i}} + \cos\chi\,\hat{\boldsymbol{j}}, \tag{2.12}$$

https://doi.org/10.1017/jfm.2012.1 Published online by Cambridge University Press

where tangent angle $\chi(s,t) = \tan^{-1}(\partial_s Y(s,t)/\partial_s X(s,t))$. Using the definition of the position vector of a point on $\mathscr{C}$, (2.8), the velocity and acceleration vectors are defined by

$$\boldsymbol{V}(s,t) = V_x\hat{\boldsymbol{i}} + V_y\hat{\boldsymbol{j}} = \boldsymbol{V}_o(t) + \partial_t \boldsymbol{r}(s,t), \tag{2.13}$$

$$\boldsymbol{A}(s,t) = A_x\hat{\boldsymbol{i}} + A_y\hat{\boldsymbol{j}} = \boldsymbol{A}_o + \partial_{tt}\boldsymbol{r}(s,t), \tag{2.14}$$

where $\boldsymbol{V}_o, \boldsymbol{A}_o$ are determined from (2.6). Note that $\partial_t \equiv \partial/\partial t$, and in the absence of spatial variation, $\partial_t \equiv \mathrm{d}/\mathrm{d}t$.

The reason for the apparently complicated definitions and the requirement of three points of reference is that we solve for motion of a flexible body that is allowed to translate and rotate in two-dimensional space. Flexible deflections occur due to biological processes within the body; here we represent the internal action simply by prescribing $y_1(s,t)$, the flexible-body deflection. The Lagrangian coordinate, s, with which curve $\mathscr{C}$ is parameterised, is the natural coordinate to use for two primary reasons. First, the length preservation criterion can be simply applied; second, the lateral motion of the body generated as an outcome of the internal distributed muscular processes is best described using a Lagrangian coordinate. However, since the equations of motion are most conveniently solved in a fixed frame, we need to define all points on $\mathscr{C}$ with respect to the centre of mass of the system. The steps involved are to establish the position of each point on the body with respect to the reference point, P', on curve $\mathscr{C}$ and then to determine the centre of mass, P, in the local body frame of reference. We next find the position of the centre of mass in the inertial frame, which is determined by solving for the incremental change in $\boldsymbol{R}_o(t)$ and $\theta(t)$ over the previous time step, by solving the equations of motion. We can then locate the position of the body reference point and the orientation of the body in space; consequently the position of every point on $\mathscr{C}$ is known. The steps of this algorithm are outlined in appendix A.

2.3. *Equations of motion*

The governing equations for the self-propelled fish moving in a fluid are formed by applying momentum conservation. In this system the fluid force contribution must balance the time rate of change of linear and angular momentum of the fish as it dynamically responds to a prescribed time-varying bend. The fluid models used in this work are discussed in detail in § 3; in this section their contribution is represented by fluid force and yaw moment vectors,

$$\boldsymbol{f}_f(s,t) = f_{f,x}(s,t)\,\hat{\boldsymbol{i}} + f_{f,y}(s,t)\hat{\boldsymbol{j}} \tag{2.15}$$

and

$$\boldsymbol{M}_f = M_f(s,t)\,\hat{\boldsymbol{k}} = (\boldsymbol{X}(s,t) - \boldsymbol{R}_o(t)) \wedge \boldsymbol{f}_f(s,t) \tag{2.16}$$

respectively. The linear and angular momentum conservation conditions can now be enforced. As discussed, flexible motion is prescribed and so the only variables in the problem are the rigid-body terms, $R_x(t), R_y(t), \theta(t)$; thus if we factor out the spatial variation by integrating over the body length the equations of motion are

$$\int_0^l (\boldsymbol{f}_f(s,t) - m_b(s)\boldsymbol{A}(s,t))\,\mathrm{d}s = 0, \tag{2.17}$$

$$\int_0^l (\boldsymbol{X}(s,t) - \boldsymbol{R}_o) \wedge (\boldsymbol{f}_f(s,t) - m_b(s)\boldsymbol{A}(s,t))\,\mathrm{d}s = 0. \tag{2.18}$$

https://doi.org/10.1017/jfm.2012.1 Published online by Cambridge University Press

From (2.8)–(2.10), the variables R_x, R_y, θ are implicitly present in the system of equations. These rigid-body variables are purely functions of time, thus the governing equations can be developed as ordinary differential equations in terms of these variables. Prior to the manoeuvre, the fish is gliding with uniform speed U, along $-\hat{\boldsymbol{i}}$. Thus the initial conditions are

$$R_x(0) = 0, \quad R_y(0) = 0, \quad \theta(0) = 0, \tag{2.19}$$

$$\dot{R}_x(0) = -U, \quad \dot{R}_y(0) = a, \quad \dot{\theta}(0) = b, \tag{2.20}$$

where a and b depend on the problem under consideration (dotted variables indicate the temporal derivative ∂_t). With expressions for the fluid-dynamic contribution, the problem definition is complete.

3. Modelling the fluid dynamics

Two fluid models are examined in this section. In § 3.1, Model 1 is developed using the elongated-body theory of Lighthill (1960) with the correction for vortex shedding developed by Wu (1971*b*). Although this approach is an adequate representation of the fluid dynamics for small deformations this linear model neglects two key nonlinear effects: large-amplitude deformations and the nonlinear upstream-induced effects of the wake vortex sheet on the body as it is moves in space. In § 3.2 we discuss Model 2, a boundary-element method that accounts for the above-mentioned nonlinear effects. It is worth noting that Model 1 is developed with a two-fold purpose: (i) in the limit of small deformations, it serves as an independent method to validate the numerical Model 2 and (ii) the analytical formulation allows us to gain some physical insights into factors that can influence the swimmer's manoeuvrability.

3.1. *Model 1: elongated-body theory with vortex shedding*

The elongated-body theory developed by Lighthill (1960) was derived in the frame of reference of the fish, moving with speed $U(t)$ along $-\boldsymbol{e_x}$. This gives an expression for the normal reactive force exerted by the fluid on the fish:

$$f_n(s,t) = -\left(\frac{\partial}{\partial t} + U\frac{\partial}{\partial s}\right) m_a(s) V_n(s,t), \tag{3.1}$$

where

$$U(t) = -\boldsymbol{V}_o(t) \cdot \boldsymbol{e_x}(t), \quad V_n(s,t) = \boldsymbol{V}(s,t) \cdot \boldsymbol{n}(s,t) \tag{3.2}$$

and $m_a(s)$ is the added mass (per unit body length), where by Lighthill's explanation the added mass is 'approximately the mass of the circular cylinder of water of diameter equal to the depth of the body at cross-section, while moving in the transverse y direction'. Thus for a body of depth d, $m_a(s) = \pi/4 d^2(s)$.

The elongated-body theory is based on slender-body theory (Batchelor 1967), which is valid for bodies with length dimensions significantly larger than the maximum cross-wise dimension, with slowly varying cross-sectional area and making small-amplitude deformations. In a significant step towards an analytical model of swimming fish with geometric variations and wake–body interactions, Wu (1971*b*) developed an approach to analyse fish-shaped geometries with dorsal and ventral fins. By the Kutta condition infinitely thin edges of the fins shed vortices and Wu observed that the fluid dynamics of a position on the body downstream of the vortex shedding edge will be affected by these vortices. Thus the slender-body theory assumption of hydrodynamically independent cross-sections is no longer adequate and the analytical

https://doi.org/10.1017/jfm.2012.1 Published online by Cambridge University Press

model must account for this interaction. Wu addresses these issues by combining elements of elongated-body theory (Lighthill 1960) and waving-plate theory (Wu 1961). Here we briefly examine this theory with the intent to explain the origin of the hydrodynamic force expressions used in this work. It is also worth emphasising that this is a linearised theory, thus lateral deformations along $\boldsymbol{e}_y$ are small-amplitude functions of time t and position s.

The theory proposed by Wu (1971*b*) is based on the premise that in typical fish shapes the longitudinal variation of depth increases from zero at the nose, achieves an intermediate peak, and then decreases towards the caudal peduncle, with dorsal and ventral fins situated aft of peak span. This particular geometry guides the fluid-dynamic model required at a particular cross-section. The fluid dynamics ahead of edges that shed vortices are modelled using elongated-body theory, whereas aft of peak span the model includes interactions with the vortex wake sheet shed at a prior longitudinal position at an earlier instant in time; in accordance with the Kutta condition the velocity is discontinuous but the pressure is continuous across the wake sheet. The flow field is expressed in terms of the velocity $\tilde{\phi}$ and acceleration (Φ) potential functions, where velocity perturbation $\boldsymbol{v} = \nabla\tilde{\phi}$ and acceleration potential $\Phi = (p_\infty - p)/\rho$ (p is the pressure, ρ is the fluid density, subscript ∞ refers to background flow variables). The linearised Euler equations are satisfied for solutions of the Laplacian, the Laplace variable being $\tilde{\phi}$ ahead of peak span and Φ aft of peak span. By the condition of linear momentum conservation these potential functions are related by $\Phi = \mathrm{D}\tilde{\phi}$ where operator $\mathrm{D} = \partial_t + U_\infty\partial_s$. For prescribed body deflections, $h(s, t)$, the exact solutions are found by satisfying the following equations at the boundary:

$$\partial_z\tilde{\phi}|_{y\to 0^\pm} = \mathrm{D}h(s, t), \tag{3.3}$$

$$\partial_z\tilde{\Phi}|_{y\to 0^\pm} = \mathrm{D}^2h(s, t), \tag{3.4}$$

noting from the definitions presented earlier in this description that (3.3) implies (3.4) but not the reverse. Thus equations (3.3) and (3.4) are solved ahead of and aft of peak span respectively. The pressure difference across the body $\Delta p = [\Phi]^\pm$ is integrated at each cross-section in $\pm z(x)$. For symmetric geometries, the algebra simplifies to the following expression for the normal force per unit length:

$$f_n = -\left(\frac{\partial}{\partial t} + U\frac{\partial}{\partial s}\right) m_a(s)V_n(s, t) + \epsilon_1 UV_n(s, t)\frac{\partial m_a(s)}{\partial s}, \tag{3.5}$$

where ϵ_1 is either 1 or 0 depending upon whether the cross-section corresponds respectively to a wake shedding edge or not.

We are now in a position to apply this model to analyse flexible manoeuvres in simple symmetric geometries. Kambe (1978) employed (3.5) to model self-propulsion in a rigid fish; here we extend his approach to model self-propulsion in a flexible fish. Thus accounting for flexible motion, the normal component of the velocity vector is given by

$$V_n(s, t) = -V_x \sin\chi + V_y \cos\chi. \tag{3.6}$$

Thus $\partial_t V_n(s, t) = \boldsymbol{A}\cdot\boldsymbol{n} - \partial_t\chi V_\tau$ and $\partial_s V_n(s, t) = \partial_t\chi - \partial_s\chi V_\tau$, where $V_\tau = \boldsymbol{V}\cdot\boldsymbol{\tau}$ and $\boldsymbol{A}$ is given by (2.14). Now the normal force distribution can be written in vector form as

$$\boldsymbol{f}_f(s, t) = -\big(m_a(\boldsymbol{A}\cdot\boldsymbol{n} + U\partial_t\chi - V_\tau(\partial_t\chi + U\partial_s\chi)) + m_a'(s)(1-\epsilon_1)UV_n\big)\,\boldsymbol{n} \tag{3.7}$$

(primed terms correspond to the spatial derivative ∂_s). The expression (3.7) is substituted in the governing equations (2.17)–(2.18), which when written in standard

https://doi.org/10.1017/jfm.2012.1 Published online by Cambridge University Press

form give

$$\left(\begin{array}{c|c} \mathbb{I}_{3\times3} & \mathbb{O}_{3\times3} \\ \hline \mathbb{O}_{3\times3} & \mathbb{A} \end{array}\right)\dot{\boldsymbol{\xi}} = \left(\begin{array}{c|c} \mathbb{O}_{3\times3} & \mathbb{I}_{3\times3} \\ \hline \mathbb{O}_{3\times3} & \mathbb{B} \end{array}\right)\boldsymbol{\xi} + \left(\begin{array}{c} \boldsymbol{O}_{3\times1} \\ \hline \boldsymbol{C} \end{array}\right), \tag{3.8}$$

where the variable vector $\boldsymbol{\xi} = [R_x\, R_y\, \theta\, \dot{R}_x\, \dot{R}_y\, \dot{\theta}]^{\mathrm{T}}$, and coefficient matrices $\mathbb{A} = \mathbb{A}_m - \mathbb{A}_f, \mathbb{B} = -(\mathbb{B}_m - \mathbb{B}_f), \boldsymbol{C} = -(\boldsymbol{C}_m - \boldsymbol{C}_f)$. Body inertia matrices are indicated by subscript m,

$$\mathbb{A}_m = \begin{pmatrix} M_b & 0 & -a_{x,1} \\ 0 & M_b & a_{y,1} \\ -a_{z,x} & a_{z,y} & a_{z,1} \end{pmatrix}, \quad \mathbb{B}_m = \begin{pmatrix} & & -a_{x,2} \\ \mathbb{O}_{3\times2} & & a_{y,2} \\ & & a_{z,2} \end{pmatrix}, \quad \boldsymbol{C}_m = \begin{pmatrix} a_{x,3} \\ a_{y,3} \\ a_{z,3} \end{pmatrix} \tag{3.9}$$

and the fluid matrices by subscript, f,

$$\mathbb{A}_f = \begin{pmatrix} a_4 & a_5 & a_6 \\ b_4 & b_5 & b_6 \\ c_4 & c_5 & c_6 \end{pmatrix}, \quad \mathbb{B}_f = \begin{pmatrix} a_1 & a_2 & a_3 \\ b_1 & b_2 & b_3 \\ c_1 & c_2 & c_3 \end{pmatrix}, \quad \boldsymbol{C}_f = \begin{pmatrix} a_0 \\ b_0 \\ c_0 \end{pmatrix}. \tag{3.10}$$

Coefficients $a_i, b_i, c_i, a_{x,i}, a_{y,i}, a_{z,i}$ are defined in appendix B, $\mathbb{I}_{p\times q}$ and $\mathbb{O}_{p\times q}$ represent the identity and zero matrices respectively, of size $p \times q$. Elements in $\mathbb{A}$ and $\mathbb{B}$ are the linear coefficients of the body inertia and fluid dynamic force (or at most sine and cosine functions in θ), whereas $\boldsymbol{C}$ contains the nonlinear contribution of inertia and the fluid dynamics. The system of equations is solved numerically using the Runge–Kutta method with the `ode45` solver in MATLAB. Specific details with respect to the choice of $m_a(s), m_b(s)$, initial conditions and prescribed functions are discussed for the various cases studied in §§ 4 and 5.

3.2. *Model 2: numerical boundary-element method*

In this section we outline the implementation of the numerical boundary-element method that was developed to model a flexible swimming fish. The method is computationally efficient and a typical approach in problems that model moving boundaries. In applications to fish swimming problems, studies typically employ a source-dipole boundary-element method to model bodies of finite thickness (Wolfgang *et al.* 1999) or the vortex ring method to model infinitely thin bodies (Cheng, Zhuang & Tong 1991). Both methods use the unsteady Bernoulli equation to derive an expression for the fluid force acting on the fish due to prescribed flexible-body deflections. The rigid-body response to the hydrodynamic pressure was modelled by Hill (1998) and he extended Cheng *et al.*'s model to include large-amplitude motion in a self-propelled fish. In this work we follow Hill's approach – in § 3.2.1 we discuss the numerical formulation of the vortex ring method. The principal difference from Hill's model is that we no longer assume the mass as being concentrated at P'; instead we explicitly calculate the instantaneous position of the centre of mass, P, at each time step as given by the approach developed in § 2. This is particularly important for bends of large amplitude. In § 3.2.2 the expression for the unsteady pressure difference across the body is defined in terms of the body velocity and local vorticity strength induced on each panel. Expressions for the fluid-dynamic force and moment are given in terms of the pressure difference across the body and the suction thrust at the leading edge of the thin plate. Substitution of the fluid-dynamic contribution into the equations of motion, (2.17)–(2.18), yield the governing equations for Model 2. In appendix C we discuss the convergence of the numerical method.

https://doi.org/10.1017/jfm.2012.1 Published online by Cambridge University Press

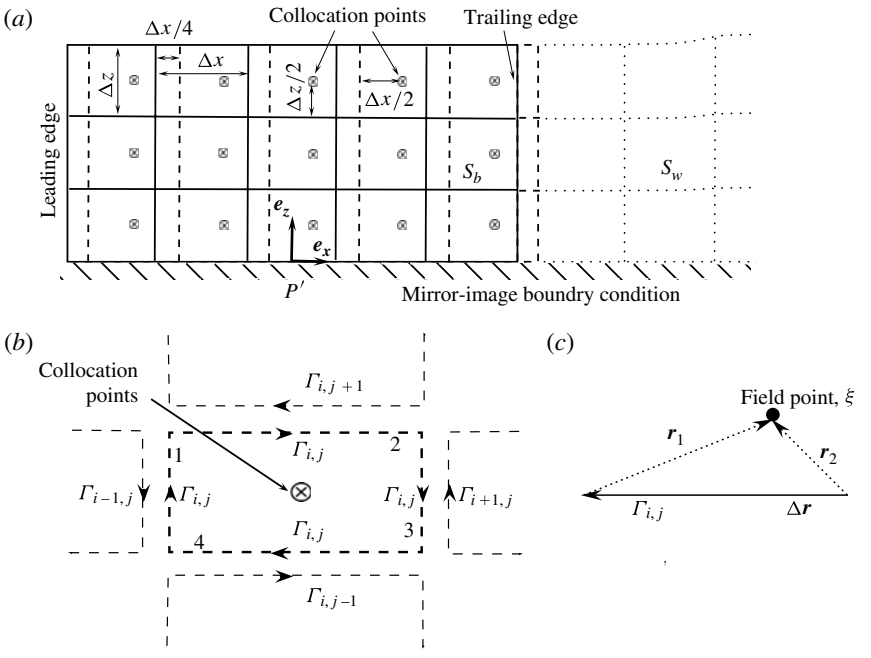


FIGURE 2. Schematic of the numerical model developed in § 3.2: (*a*) The rectangular fish (S_b) discretised into rectangular elements (solid lines) of uniform length Δx and width Δz. Each body element is associated with a vortex ring (dashed lines) positioned a distance $\Delta x/4$ behind the element leading edge. The wake vortex sheet, S_w (dotted lines) is derived from previously shed body line elements. (*b*) The (i, j)th vortex ring is described (thick dashed lines) by its four line elements of strength $\Gamma_{i,j}$ with a centrally located collocation point. Neighbouring vortex rings (thin dashed lines) are also shown, with reference to terms in (3.16). (*c*) Definition of the terms in the expression (3.13) for the induced velocity at field point ξ due to a line vortex element of strength $\Gamma_{i,j}$.

3.2.1. *Vortex ring method*

In figure 2 we sketch the fish as modelled in this work: the fish is assumed to be an infinitely thin rectangular surface, S_b, modelled with a distribution of $N_x \times N_z$ discrete elements. Each element is associated with a rectangular vortex ring, the edges of the ring being line vortex elements, the strengths of which are computed at each time instant. For computational efficiency, the half-body is modelled and mirror-symmetry boundary conditions are applied. At each time step the body sheds an elemental wake vortex, so that the shed wake surface, S_w, grows in time (see figure 2*a*). The fluid is incompressible, inviscid and bounded by surfaces S_b, S_w and the boundary at infinity. The flow is irrotational everywhere except on S_b and S_w. Each finite element or 'panel' (on the body, S_b, or wake surface, S_w) induces a velocity field. Thus the velocity of a point on the body of the fish is the linear combination of velocity due to its own motion ($\boldsymbol{V}$, given by (2.13)) and that induced by S_b ($\boldsymbol{V}^m$) and S_w ($\boldsymbol{V}^w$), which must be determined at each time step. The boundary conditions for this system are the near-field no-penetration boundary condition and the far-field constraint, which requires that as $r \to \infty$, $\boldsymbol{V}^m$, $\boldsymbol{V}^w \to 0$ rapidly. Mass conservation requires

$$\nabla \cdot \boldsymbol{V}^m = 0, \quad \nabla \cdot \boldsymbol{V}^w = 0. \tag{3.11}$$

https://doi.org/10.1017/jfm.2012.1 Published online by Cambridge University Press

Line vortex elements that model the body and wake surfaces naturally satisfy (3.11). The no-penetration boundary condition requires that the normal component of induced velocity due to the body, $\boldsymbol{V}^m$, matches normal components of velocities due to motion of the body, $\boldsymbol{V}$, and induced velocity field due to the wake, $\boldsymbol{V}^w$,

$$\boldsymbol{V}^m \cdot \boldsymbol{n} = (\boldsymbol{V} - \boldsymbol{V}^w) \cdot \boldsymbol{n}. \tag{3.12}$$

The circulation strength of each elemental ring is determined from this velocity boundary condition and (3.12) is solved in discrete form at each time instant. The solution of this equation forms the crux of this particular boundary element method.

The numerical algorithm involves a two-step solution: in the inner step we determine the induced velocity fields, $\boldsymbol{V}^m$, $\boldsymbol{V}^w$, where the body velocity vector, $\boldsymbol{V}$, includes the prescribed contribution due to flexible-body motion and an assumed solution for the rigid-body terms. In this step we formulate the discrete system of equations to determine the spatial variation of the induced velocity field. The pressure difference across the body is determined using the unsteady Bernoulli theorem, and surface integration yields expressions for the fluid force. In the outer step, the rigid-body variables (R_x, R_y, θ) are determined from the solution of the governing equations (2.17)–(2.18). The solver proceeds iteratively until rigid-body solutions satisfy the equations of motion within an allowable relative error of 10^{-6}.

Formulation of the discrete system of equations

The discretisation of (3.12) follows the standard approach (see for instance Lan 1979; Cheng, Pedley & Altringham 1998; Katz & Plotkin 2001); thus here we briefly describe the key steps involved in obtaining the discrete system of equations of motion. Each panel is associated with a vortex ring: in figure 2(*b*) each vortex ring is composed of four line vortex segments of strength $\Gamma_{i,j}$ and a centrally located collocation point. By the Biot Savart law a finite line vortex (of length $|\Delta \boldsymbol{r}| = |\boldsymbol{r}_2 - \boldsymbol{r}_1|$) of strength $\Gamma_{i,j}$, induces a velocity at a field point ξ:

$$\boldsymbol{q}(\xi, t) = \frac{\Gamma_{i,j}}{4\pi} \frac{\boldsymbol{r}_1 \wedge \boldsymbol{r}_2}{(|\boldsymbol{r}_1 \wedge \boldsymbol{r}_2| + r_{core}^2)} \Delta \boldsymbol{r} \cdot \left(\frac{\boldsymbol{r}_1}{r_1} - \frac{\boldsymbol{r}_2}{r_2} \right); \tag{3.13}$$

$\boldsymbol{r}_1, \boldsymbol{r}_2$ are position vectors of the ends of the line vortex segment with respect to field point ξ and r_{core} is a desingularising parameter introduced to ensure the system is well-posed (terms in (3.13) are illustrated in figure 2*c*).

The method of desingularisation adopted in (3.13) addresses the singular limit of $r_1, r_2 \to 0$ which causes the system of equations to become ill-posed. We have followed prior numerical work on this (Hill 1998; Wolfgang *et al.* 1999) where the desingularising approach proposed by Krasny (1986) is implemented. Krasny introduced a length scale to represent the viscous core radius of the line vortex element. This length scale, r_{core}, removes the singularity and effects a smoothing of the solutions. Careful numerical tests are employed to ensure this smoothing does not lead to spurious values of the pressure, and a value of $r_{core} = 1 \times 10^{-6}/N_x$ was selected based on the criteria for pressure convergence (see Hill 1998, for details).

The discrete form of (3.12) leads to a system of equations that are defined in terms of the elemental vortex ring strength. Redefining the numbering to distinguish bound and collocation points, the lth element represents the collocation point at which the influence coefficient due to all other m elements is calculated, where l, m vary from 1 to $N_x \times N_z$. For $N = N_x \times N_z$ vortex rings of unknown strength Γ_l the discrete system

https://doi.org/10.1017/jfm.2012.1 Published online by Cambridge University Press

of equations is given by

$$\sum_{m=1}^{N} Q_{l,m}\Gamma_l = (\boldsymbol{V}_l - \boldsymbol{V}_l^w)\cdot\boldsymbol{n}_l, \quad l = 1\ldots N, \tag{3.14}$$

where $\boldsymbol{V}_l\cdot\boldsymbol{n}_l$ and $\boldsymbol{V}_l^w\cdot\boldsymbol{n}_l$ are respectively the normal component of the body velocity and the induced velocity due to the wake vortex sheet. Thus $\mathbb{Q}$ is the $N\times N$ influence coefficient matrix where element $Q_{l,m}$ corresponds to the normal component of induced velocity at the lth collocation point due to the mth vortex ring of unit strength. From figure 2(*b*) we note that each ring is composed of four vortex segments where arrows show the positive sense for the vorticity vector. And so,

$$Q_{l,m} = (\boldsymbol{q}^1 + \boldsymbol{q}^2 - \boldsymbol{q}^3 - \boldsymbol{q}^4)_{l,m}\cdot\boldsymbol{n}_l, \tag{3.15}$$

where $(\boldsymbol{q}^k)_{l,m}$ refers to the velocity induced at the lth collocation point due to the kth line vortex segment in the mth ring, where k corresponds to the numbering of line vortex segments as indicated in figure 2(*b*). The expression for $\boldsymbol{q}^k$ is computed using (3.13). This linear system (3.14) is solved in terms of Γ_l and the instantaneous body-bound vorticity field is determined at each time step. Note that the index l must not be confused with the non-dimensional body length.

Model of the wake vortex sheet

The Kutta condition requires that the fluid leave the trailing edge smoothly and for unsteady motion this means that at each time instant a zero pressure difference is required across the trailing edge. To satisfy this criterion we employ the standard technique of modelling a vortex shed at each instant in time. In a two-dimensional system of point vortices, the Kutta condition requires that a point vortex is shed at the trailing edge. The strength of the instantaneously shed vortex is determined from the Kelvin–Helmholtz theorem, which requires that the rate of change of total circulation around the body and the wake is zero. To model the flat plate of finite aspect ratio we assume that this process is approximately two-dimensional, and corresponding to each trailing spanwise panel line vortices are shed, where the most recently shed line vortex strength is equal in magnitude to the trailing ring vortex strength at the previous time step. In time these line vortices collectively describe a wake vortex sheet, S_w. The vorticity shed by the body is confined to S_w, and the sheet propagates downstream from the body as it grows and evolves due to the induced velocity field of neighbouring vortices (see figure 2*a*). The wake shedding model and evolution of the vortex sheet follows standard panel method techniques, a detailed description of which can be found in Wolfgang *et al.* (1999). It is worth noting that in our model only the trailing edge is the wake shedding edge; vortices shed from side edges will be included in subsequent work.

3.2.2. *Expression for the fluid-dynamic force and moment*

The bound vorticity strength for each elemental vortex ring, $\Gamma_{i,j}$, is determined by solving (3.14) and computing the induced velocity vector, $\boldsymbol{V}^w$, generated by the evolving surface, S_w. These computations are performed at each time step. The pressure difference across the body is determined by applying the unsteady Bernoulli equation, as derived for a flexible swimmer by Hill (1998) on the basis of the formulation of Katz & Plotkin (2001). Thus for a rectangular plate of N_x chordwise and N_z spanwise elements, the pressure difference at the (i,j)th element is given by

$$\frac{\Delta p_{i,j}(t)}{\rho} = (\boldsymbol{V}^m + \boldsymbol{V}^w - \boldsymbol{V})_{i,j}\cdot\left(\boldsymbol{\tau}^x_{i,j}\frac{\Gamma_{i,j}-\Gamma_{i-1,j}}{\Delta x_{i,j}} + \boldsymbol{\tau}^z_{i,j}\frac{\Gamma_{i,j}-\Gamma_{i,j-1}}{\Delta z_{i,j}}\right) + \frac{\partial\Gamma_{i,j}}{\partial t}, \tag{3.16}$$

https://doi.org/10.1017/jfm.2012.1 Published online by Cambridge University Press

where $\boldsymbol{V}^m, \boldsymbol{V}^w, \boldsymbol{V}$ are, respectively, the body-induced, wake-induced and the body velocity vectors at the (i,j)th element of the body. $(\boldsymbol{\tau}^x_{i,j}, \boldsymbol{\tau}^z_{i,j})$ are the element tangential unit vectors along x and z directions respectively.

We apply first-order Euler integration in the spatial dimensions to obtain expressions for the total fluid-dynamic force $(\mathscr{F}_{f,x}(t), \mathscr{F}_{f,y}(t))$ and moment $(\mathscr{M}_{f,z}(t))$:

$$\mathscr{F}_{f,x}(t) = \sum_{i=1}^{N_x}\sum_{j=1}^{N_z}\left(\Delta p_{i,j}\Delta x_{i,j}\boldsymbol{n}_{i,j} - \delta_{i,1}\boldsymbol{T}^s_j\right)\cdot\hat{\boldsymbol{i}}\Delta z_{i,j}, \tag{3.17a}$$

$$\mathscr{F}_{f,y}(t) = \sum_{i=1}^{N_x}\sum_{j=1}^{N_z}\left(\Delta p_{i,j}\Delta x_{i,j}\boldsymbol{n}_{i,j} - \delta_{i,1}\boldsymbol{T}^s_j\right)\cdot\hat{\boldsymbol{j}}\Delta z_{i,j}, \tag{3.17b}$$

$$\mathscr{M}_{f,z}(t) = \sum_{i=1}^{N_x}\sum_{j=1}^{N_z}\left(\boldsymbol{X}(s_{i,j},t) - \boldsymbol{R}_o(t)\right)\wedge\left(\Delta p_{i,j}\Delta x_{i,j}\boldsymbol{n}_{i,j} - \delta_{i,1}\boldsymbol{T}^s_j\right)\cdot\hat{\boldsymbol{k}}\Delta z_{i,j}. \tag{3.17c}$$

The Kronecker delta, $\delta_{i,1}$, indicates that suction thrust $(\boldsymbol{T}^s_j)$ contributions arise only from the sharp leading edge (at $i=1$). Expressions for suction thrust in finite-depth bodies are determined using the approach developed by Robinson & Laurmann (1956) who extended Blasius' expression for suction thrust in two-dimensional thin aerofoils to three-dimensional finite-depth aerofoils. For the straight leading edge of rectangular plates, the suction thrust per unit length at a spanwise point on the leading edge is given as

$$T^s(x) = \pi C^2(x) \tag{3.18}$$

where

$$C(x) = \lim_{x\to 0}\sqrt{x}\,\boldsymbol{u}_o\cdot\boldsymbol{\tau}. \tag{3.19}$$

Note that $\boldsymbol{u}_o$ is the local velocity in the neighbourhood of the leading edge. Writing (3.18) for the discrete system, the leading-edge suction thrust per unit length for the jth leading panel is

$$\boldsymbol{T}^s_j = \pi C^2_j\boldsymbol{\tau}^x_{1,j} \tag{3.20}$$

where

$$C_j = \left(\frac{\Gamma_{1,j}}{\Delta x_{1,j}} + (\boldsymbol{V}^m_{1,j} + \boldsymbol{V}^w_{1,j})\cdot\boldsymbol{\tau}^x_{1,j}\right)\sqrt{a_{LE}\Delta x_{1,j}}. \tag{3.21}$$

The term a_{LE} in (3.21) is the radius of the circle of infinitesimal radius at which the leading-edge suction term is computed. Using results from the study by Hill (1998) we fix $a_{LE} = 0.32$. The element length and depth dimensions of the jth spanwise element at the leading edge are respectively $\Delta x_{1,j}, \Delta z_{1,j}$. This numerical approach to compute the three-dimensional hydrodynamic pressure requires $(N_xN_z)\times(N_xN_z)$ matrix inversions for N_t time steps, for a swimmer discretised with N_x chordwise and N_z spanwise panels.

3.2.3. *Equations of motion*

The equations of motion are virtually identical to those derived in (3.8)–(3.10) (for Model 1), except that the linear terms in the fluid-dynamic expressions are implicit in the numerical computation and so we incorporate the entire contribution of the

https://doi.org/10.1017/jfm.2012.1 Published online by Cambridge University Press

fluid dynamics in the nonlinear vector $\boldsymbol{C}_f^{num}$. Thus for Model 2 we solve the following system of equations:

$$\left(\begin{array}{c|c} \mathbb{I}_{3\times3} & \mathbb{O}_{3\times3} \\ \hline \mathbb{O}_{3\times3} & \mathbb{A}_m \end{array}\right)\dot{\boldsymbol{\xi}} = \left(\begin{array}{c|c} \mathbb{O}_{3\times3} & \mathbb{I}_{3\times3} \\ \hline \mathbb{O}_{3\times3} & -\mathbb{B}_m \end{array}\right)\boldsymbol{\xi} + \left(\begin{array}{c} \boldsymbol{O}_{3\times1} \\ \hline \boldsymbol{C}_f^{num} - \boldsymbol{C}_m \end{array}\right) \tag{3.22}$$

where

$$\boldsymbol{C}_f^{num} = \begin{pmatrix} \mathscr{F}_{f,x} \\ \mathscr{F}_{f,y} \\ \mathscr{M}_{f,z} \end{pmatrix} \tag{3.23}$$

and $\mathbb{A}_m, \mathbb{B}_m, \boldsymbol{C}_m$ and $\boldsymbol{\xi}$ are defined in § 3.1. It should be noted that the pressure difference varies along the depth and so at each time step we compute $\mathscr{F}_{f,x}, \mathscr{F}_{f,y}, \mathscr{M}_{f,z}$ from (3.17), noting that the numerical integration is performed along the depth as well as the length.

Equation (3.22) is solved numerically subject to initial conditions (2.19) and (2.20). Based on our choice of deflection functions and initial conditions and the fluid-dynamic pressure distribution, it is known that $R_x(t), R_y(t), \theta(t)$ are smooth functions in time and therefore devoid of singularities in the solution space. Thus we use the implicit Bulirsch–Stoer method to solve the system of differential equations with fourth-order accuracy. The principal advantage over the computationally more expensive (albeit robust) fourth-order Runge–Kutta method is that it is faster with equivalent accuracy. The algorithm is presented in Press *et al.* (2007) and the implementation specific to this problem is discussed in detail in Singh (2009).

4. Verification and results: manoeuvres in rigid and flexible fish

The two fluid-dynamics models developed in § 3 are applied to study two mechanisms of effecting turns. We first examine the response to a rigid-body impulse, which is the approach proposed by Kambe (1978) to model manoeuvres in rigid fish. In order to verify the implementation, in § 4.1 we compare results from Model 1 with Kambe's results. The impulse response is then applied to a rectangular-shaped fish and the results from Models 1 and 2 are compared in § 4.2. In § 4.3 a flexible deflection is prescribed to mimic the C-turn action of fish and we compare the response of both models.

4.1. *Rigid-body response to an impulse: elliptical fish*

Kambe (1978) considered a fish with an ellipse-like profile such that the longitudinal variation of the span about s_o (reference point P', see figure 1) is given by

$$d(s) = d_o\left(1 - \left(\frac{s - s_o}{s_o}\right)^2\right), \tag{4.1}$$

where d_o is the span at s_o. Here we define the reference point at mid-length ($s_o = l/2$) and so the shape is symmetric about $\boldsymbol{e}_z = 0$. In Kambe's model the action of the tail was modelled as a point force at $s = l$, implemented by applying an impulsive input to $\dot{\theta}$ and $\dot{R}_y$ at time, $t = 0$. The rigid-body response of the fish was then calculated. Thus initial conditions, (2.19) and (2.20), are

$$R_x(0) = 0, \quad R_y(0) = 0, \quad \theta(0) = 0, \tag{4.2}$$

$$\dot{R}_x(0) = -U_o, \quad \dot{R}_y(0) = I_o, \quad \dot{\theta}(0) = 7I_o. \tag{4.3}$$

https://doi.org/10.1017/jfm.2012.1 Published online by Cambridge University Press

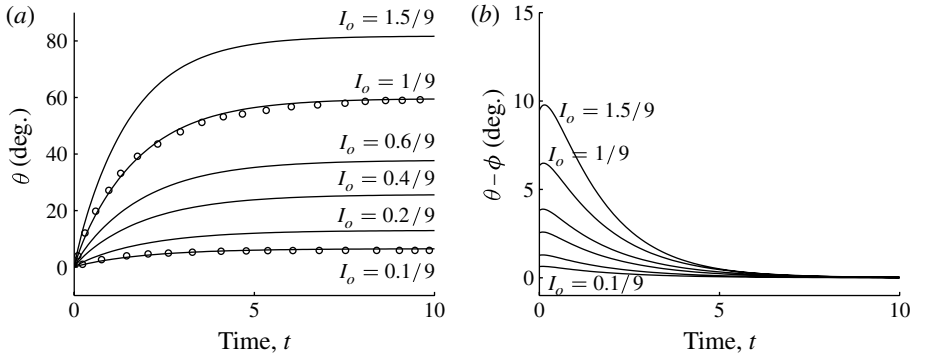


FIGURE 3. Rigid-body turns by a fish with an elliptical profile ($d_o = 0.6$): variation in time of (*a*) θ, turn response, and (*b*) $\theta - \phi$, the orientation relative to the direction of swimming, due to an impulsive action of strength $9I_o = 0.1$–1.5 as given in (4.2) and (4.3). In (*a*), Kambe's predictions for the purely reactive response are compared (circles).

I_o is varied from 0.1/9 to 1.5/9. For this and subsequent calculations, we prescribe the initial motion of the fish with a speed $U_o = 1$. For other parameters we use Kambe's values, which correspond to added mass, $m_a(s) = \pi/4d(s)^2$, inertial mass, $m_b = 0.6\pi/4d(s)^2$, and $d_o = 0.6$.

In figure 3 we plot the variation in time of θ, the orientation of the body with respect to the initial swimming direction $\hat{\boldsymbol{i}}$, and $\theta - \phi$, the angle between the relative fluid velocity and the body orientation, for increasing values of impulse strength, I_o. We choose the range of allowable I_o to ensure turn angle values do not exceed $\pi/2$. In figure 3(*a*) we include the two cases of the purely reactive response computed by Kambe (corresponding to impulsive inputs $9I_o = 0.1$ and 1). The agreement is good and as Kambe predicted, θ asymptotes to a steady value which scales directly with I_o and $\theta - \phi$ decays to zero for large times (figure 3*b*).

It is worth emphasising that the geometry of the caudal fin is not modelled in Kambe's analysis. Although the role of the finite-depth tail during swimming is well understood, recent work on manoeuvres suggest that the tail is actively employed during turning as well. Furthermore, ray-finned fish have the ability to dynamically change the fin surface area; these biological observations motivate us to analyse the role of body geometry in manoeuvres and so we analyse the turn response of the rectangular-shaped fish next.

4.2. *Rigid-body response to an impulse: rectangular fish*

Here we consider the response of a rectangular-shaped fish (depth $d = 0.6$) to an impulsive input and compare predictions from the two fluid-dynamic models (Models 1 and 2) developed in § 3. The objective of this section is twofold: (i) to cross-verify the two models and (ii) to understand the role of body geometry in the turn response. For this geometry, the inertia per unit length is given as $m_b = d$. To define the added mass for Model 1, we need to consider the geometry a little carefully. As discussed in § 3, Model 2 accounts for the singularity at the trailing edge by modelling the shed wake. In Model 1 we need to explicitly account for this abrupt change in slope at leading and trailing edges, and we do so by applying a sigmoidal function at these two ends. Thus we define

$$m_a(s) = \frac{\pi d^2}{2}\left(1 - \frac{2}{1 + \mathrm{e}^{-\alpha(s-s_i)}}\right)(s_i - s_o). \tag{4.4}$$

https://doi.org/10.1017/jfm.2012.1 Published online by Cambridge University Press

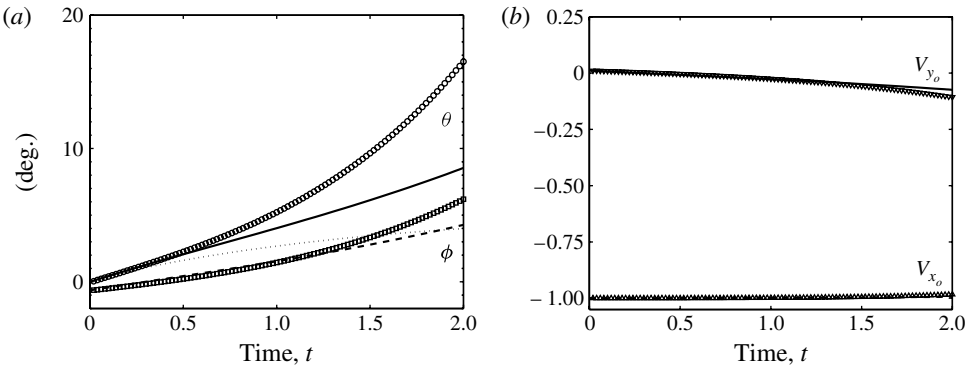


FIGURE 4. (*a*) The time-varying response of θ and ϕ to an impulsive input of strength $I_o = 0.1/9$ (see (4.2) and (4.3)) for a rectangular-shaped fish of depth $d = 0.6$. Model 1 response (solid and dashed curves for θ, ϕ respectively) is compared with the Model 2 prediction (θ: circles, ϕ: squares). The dotted line corresponds to the θ response from figure 3(*a*) for an identical input to an elliptical body. (*b*) The rigid-body velocity variation, V_{x_o}(inverted triangles) and V_{y_o} (triangles) in time.

where $s_i = 0$ or 1. The dependence on the parameter α was checked to ensure solutions asymptote to a fixed response. Based on these checks we settled on a value of $\alpha = 400$ (corresponding to which θ, ϕ are less than 3 % of the asymptotic value, so we maintain this value for all subsequent calculations).

The system of equations is solved as discussed in the previous section. We compute the rigid-body response to an impulse of $I_o = 0.1/9$ (initial conditions as defined in (4.2) and (4.3)) and in figure 4(*a*) we plot θ and ϕ. We examine these results keeping in mind the two stated objectives of this section. In terms of cross-verifying the two models we find that the predictions from both models agree well for early times ($t \sim 1$); however the error between models increases over time. The chief difference between the two models is the induced effect of the near wake on the body. As the side-slip, V_{yo}, increases, the strength of the wake circulation increases in time, thereby enhancing the turn response. This nonlinear wake effect is not included in Model 1, thus the difference between the two solutions grows in time. Despite this issue, the trends are close initially and for manoeuvres where the response at initial times is important for the fish, Model 1 may be considered to be adequate.

In order to understand the role of geometry we contrast the response of the elliptical fish with that of the rectangular fish for the same impulsive input of $I_o = 0.1/9$. The mechanism contributing to this motion may be understood by examining the response of ϕ with respect to θ (or the lateral rate of side-slip, V_{y_o}, with respect to longitudinal velocity, V_{x_o}). The plots in figure 4(*a*) show that as the fish turns it also side-slips, which leads to an enhanced pressure difference across the body. Furthermore, due to asymmetry induced from boundary conditions at the nose and tail, $\partial_s m_a(0)$ is positive and large for the rectangular fish, whereas for an elliptical shape this quantity is comparatively very small. Thus a differential torque is generated, $\dot{\theta}$ increases and the body progressively yaws. In this manner side-slip and yaw rotation feed into each other resulting in the observed large growth in rigid-body response.

Finally a note with respect to the longitudinal dynamics: as the fish rotates in space the effect on the longitudinal dynamics is much less than on the lateral or yaw dynamics. Figure 4(*b*) indicates the V_{x_o} (rigid-body velocity component

https://doi.org/10.1017/jfm.2012.1 Published online by Cambridge University Press

along $\hat{\boldsymbol{i}}$) variation in time, for which the change is much smaller than for V_{y_o} (rigid-body velocity component along $\hat{\boldsymbol{j}}$). Thus for modelling small-amplitude turns, the longitudinal dynamics may be neglected.

4.3. *Response due to a flexible bend*

Next we implement the flexible-body bend observed in fish during turns. Studies by Gray (1933) have led to the observation that direction change in a fish can be most simply effected by a C shaped bend in the body. To effect such a C-shape, we define the reference point on the body, P', at the half body length ($s_o = l/2$). We then prescribe a lateral body deflection function, $y(s, t)$, in the form:

$$y(s, t) = h_o h_1(s) g(t), \tag{4.5}$$

where h_o is a scaling factor and is a measure of the strength of the bend, whilst $h_1(s)$ describes the shape of the body bend and we select it such that the body bends symmetrically about s_o:

$$h_1(s) = \left(\frac{s - s_o}{l}\right)^2, \quad s \in (0, l). \tag{4.6}$$

The temporal component, $g(t)$, is non-zero for the duration of the turn, $t \in (0, t_o)$. However, at the end of the manoeuvre, i.e. for $t > t_o$, $g(t)$ is zero. Thus,

$$\begin{aligned} g(t) &= \frac{1 - \cos(2\pi t/t_o)}{8}, \quad t \in (0, t_o) \\ &= 0, \quad t > t_0, \end{aligned} \tag{4.7}$$

with the following initial and final conditions:

$$g = 0, \quad \dot{g} = 0, \quad \ddot{g} = \pi^2/2 \quad \text{at } t = 0 \text{ and } t_o. \tag{4.8}$$

We apply the flexible turn function (4.5) for a finite duration of time, $t \in (0, t_o)$, over which time the bend grows, then relaxes and for $t > t_o$ the fish returns to its stretched straight configuration. Inertia properties are defined as in the previous section.

Defining the bend strength in (4.5) as $h_o = 1$, the duration of the bend given by (4.7) is set at $t_o = 1$ and in figure 5(*a*) we compare the time-varying response in the orientation angle, θ, and direction of motion, ϕ. The dynamic response due to the flexible-body deflection in time interval, $0 < t < 1$, can be observed in the acceleration in the θ response during the contraction phase, $(0 < t < 0.5)$, and deceleration during the relaxation phase $(0.5 < t < 1)$; after $t = 1$ the turn response is entirely due to rigid-body interactions. This can be seen by comparing the θ and ϕ variation in time for the impulsive response examined in figure 4. The results from the two models agree quite well indicating that the inertia and pressure components dominate over the induced effects of the wake. Due to the nonlinear wake-induced effects we see the solutions diverge over time, as for the purely rigid-body turn (figure 4*a*).

In terms of understanding the role of flexible action on manoeuvrability, we see that for time $0 < t < 0.75$, a duration over which the flexible manoeuvre is effected, the direction of motion, ϕ, is negative. From figure 5(*b*), this change in sign occurs due to a small positive value of lateral side-slip, V_{y_o}, in this period. As noted from the rigid-body response, side-slip induces a flow at an angle to the body which increases the sideways motion and yaw rotation. In addition, for a symmetric flexible bend as modelled here, the first half of the body experiences a larger magnitude of relative positive side-slip, whilst for the latter part of the body, the magnitude of side-slip

https://doi.org/10.1017/jfm.2012.1 Published online by Cambridge University Press

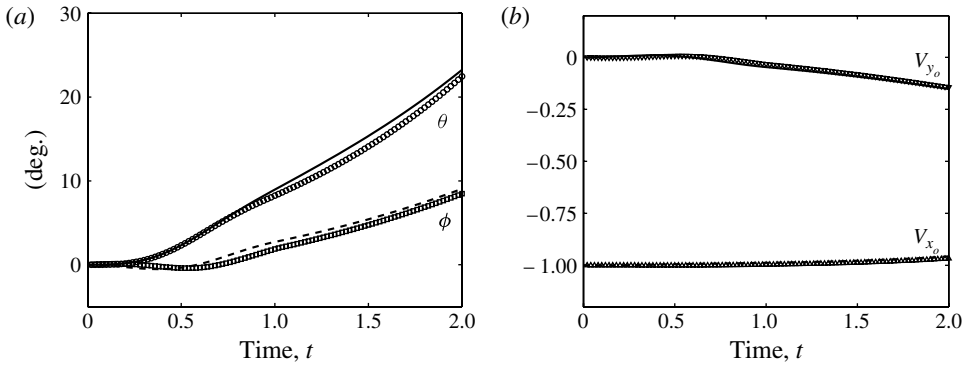


FIGURE 5. The time-varying response of (*a*) θ, ϕ and (*b*) $V_{x,o}, V_{y,o}$ are examined for a rectangular-shaped fish ($d = 0.6$) to an unsteady flexure, given by expressions (4.5)–(4.7) with $h_o = 1, t_o = 1, s_o = l/2$. Curves correspond to Model 1, symbols to Model 2 (see figure 4 for details).

reduces considerably (the increment and reduction are magnified further away from the centre of the bend). This action manifests itself as a differential fluid-dynamic torque causing a higher rate of rotation when side-slip is positive. This is consistent with the variation of the orientation angle, θ, which accelerates from $0 < t < 0.75$ and then decelerates over $0.75 < t < 1$. Thus the inertial dynamics and hydrodynamic interactions become increasingly important during manoeuvres of such a nature.

4.4. *Manoeuvrability*

The turn responses of the elliptical and rectangular fish allow us to examine the concepts of stability and manoeuvrability in particular detail. As our goal is to analyse the fluid dynamics of fish manoeuvres it is especially important to define a quantifiable measure of manoeuvrability to make useful comparisons. For the purpose of quantification we turn to the field of aeronautics where these concepts are developed more formally. In an aircraft a manoeuvre is executed by deflecting control surfaces, such as the rudder for yaw rotation, so classically the manoeuvrability of the aircraft is defined by the amount the rudder has to be deflected to achieve a certain yaw angle at a desired yaw rate (Etkin & Reid 1996). The analogy to fish swimming can now be made where for the case of a flexible bend, as for expression (4.5), the measure of the bend amplitude h_o is equivalent to a control input. The measure of the manoeuvrability is then the angle through which the fish turns over a particular time duration, or in the context of a fish chasing a predator or escaping prey, the time in which it turns through a particular angle. We must emphasise that stability and manoeuvrability are virtually opposing concepts. Stability indicates the ability of the body to resist change in its equilibrium state, whereas manoeuvrability indicates the ability to move rapidly out of a given equilibrium state. Under real conditions, it is important to be able to switch between the two states – the aircraft (or fish) must be able to exit a given state, acquire a new state and maintain its equilibrium in the new state. In figure 4 we show the turn angle due to an impulsive input to an elliptical and rectangular fish and observe that in response to an identical input, the elliptical swimmer turns through roughly 4° in 2 units of time, whilst the rectangular swimmer turns through over four times that value in the same time, suggesting superior manoeuvrability of the rectangular body. In terms of stability, the

https://doi.org/10.1017/jfm.2012.1 Published online by Cambridge University Press

elliptical swimmer asymptotes to a stable state whereas the response of the rectangular swimmer grows in time indicating that the latter geometry is inherently unstable.

The above comparison shows that not only the strength of the impulse but also the body geometry affects the stability and manoeuvrability characteristics. Observations of turns in geometrically distinct fish species corroborates the above results (Webb 1978). Ray-finned fish species control the fin area by actuating muscles at the base of the fin rays (Drucker & Lauder 2001). The advantage of dynamic extension and retraction of the fin rays during a manoeuvre can be understood in the light of the above comparisons from our numerical calculations. Thus a roughly rectangular shape (equivalent to an extended fin) is advantageous for turning the fish through large angles but for position maintenance after the desired direction is acquired, the elliptical shape (akin to a retracted tail fin) is desirable. Thus it is valid to treat the rectangular fish geometry as representative of the manoeuvring state of the fish, keeping in mind that fish have the option to retract the fin once the desired orientation is achieved, or to perform another bend to correct the overshoot – a common feature observed in fish performing sudden manoeuvres (Domenici & Blake 1997).

5. Optimising for manoeuvrability

With insights from the previous section on rigid-body and flexible turns we now employ the numerical model to understand factors that enhance manoeuvrability. In § 5.2 we examine the dependence of manoeuvrability on body depth and calculate the kinetic energy of the fish during a bend using expressions derived in § 5.1. In § 5.3 we examine how a fish might time its bend with respect to the phase of its undulatory swimming motion prior to effecting the turn so as to enhance its manoeuvrability.

5.1. *Kinetic energy of the fish*

The total kinetic energy of the fish at any instant is

$$K_{tot} = \frac{1}{2K_o} \int_0^l m_b(s) \boldsymbol{V}(s,t) \cdot \boldsymbol{V}(s,t)\, \mathrm{d}s, \tag{5.1}$$

where the energy is rescaled by the initial energy imparted $K_o = (1/2)M_b U_o^2$. Of particular interest is the energy expended by the fish in generating the flexible bend. We define this as the time-averaged energy expended,

$$K_{flex}(t) = \frac{1}{2t} \int_0^t \int_0^l m_b(s) \boldsymbol{v}_1(s,t) \cdot \boldsymbol{v}_1(s,t)\, \mathrm{d}s\, \mathrm{d}t \quad \text{for } t < t_o \tag{5.2}$$

where

$$\boldsymbol{v}_1 = \partial_t \boldsymbol{x}_1(s,t), \tag{5.3}$$

and K_{flex} saturates to the value at t_o for all times after the bend ($t \geqslant t_o$). The total energy input into the fish must include the contribution from its initial kinetic energy and so we define the scaled input energy as

$$K_{in} = 1 + \frac{K_{flex}(t_o)}{K_o}. \tag{5.4}$$

As observed from the results in the previous section, the rectangular fish continues to side-slip normal to its direction of orientation after the input action has ended. Hence the total energy does not necessarily correspond to the 'useful' energy of the fish. To address this aspect we define the 'useful' output kinetic energy as that which contributes to the propulsion of the fish in the direction of its orientation. This

https://doi.org/10.1017/jfm.2012.1 Published online by Cambridge University Press

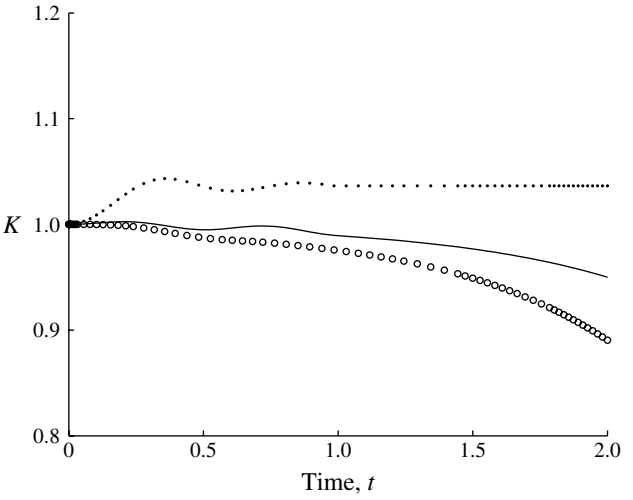


FIGURE 6. Energy of the fish corresponding to the turn modelled in figure 5: variation in time of components of kinetic energy of the fish for Model 1 are compared. K_{tot}, the fish's total kinetic energy (solid curve), K_{in}, its input kinetic energy (dots) and K_{out}, its output energy (circles).

instantaneous output kinetic energy is given by

$$K_{out}(t) = \frac{1}{2K_o} M_b \left(\boldsymbol{V}_o(t) \cdot \boldsymbol{e_x}(t)\right)^2 . \tag{5.5}$$

We now define the energy ratio computed in the time, t_{θ_f}, taken to achieve a certain target angle, θ_f,

$$K' = \frac{K_{out}(t_{\theta_f})}{K_{in}}, \tag{5.6}$$

and t_{θ_f} is computed after the initiation of the flexible bend. We note that K' is a measure of the kinetic energy retained by the fish in the process of turning and an optimal configuration is one in which the target angle, θ_f, is achieved as rapidly as possible, with as little loss of kinetic energy as possible. These two are invariably in conflict and we note that from the perspective of survival of prey from an attack by a predator a rapid escape is imperative whereas minimisation of energy loss is merely desirable.

To understand the contributions of the different components of energy for the flexible bend examined in § 4.3, in figure 6, we plot the time-varying energy components, K_{tot}, K_{in}, K_{out} given by (5.1), (5.4), (5.5) respectively. K_{in} varies over the duration of the bend and then saturates to the final value at the end of the bend, as there is no further input from the fish for times $t > t_o$. The total kinetic energy of the fish initially increases during the bend but then decays in time indicating that the fish loses energy to the fluid (due to wake dissipation). The output energy, K_{out}, decays much faster than the total kinetic energy as the lateral side-slip of the fish grows with time.

5.2. *Geometric considerations for manoeuvrability*

With the ideas of manoeuvrability developed in § 4.4 and the expressions for the energy ratio defined in § 5.1, we can formally define the measures of manoeuvrability

https://doi.org/10.1017/jfm.2012.1 Published online by Cambridge University Press

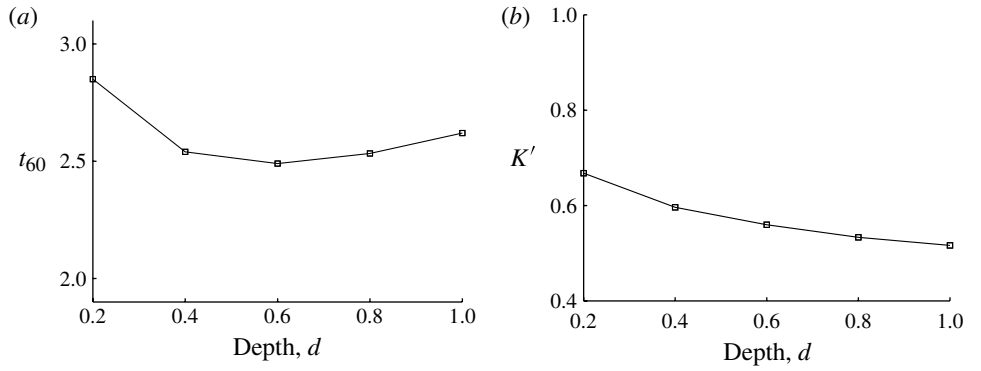


FIGURE 7. Manoeuvrability dependence on body depth, d: variation with d of (*a*) t_{60}, the time to turn through 60° and (*b*) K', the output to input energy ratio (5.6) after the turn are shown. The fish is made to perform a C-bend given by (4.5)–(4.7) ($h_o = t_o = 1$, $s_o = l/2$).

employed in this study where we compare different configurations. The goal of this study is to seek the optimal depth that achieves maximum manoeuvrability, where the measure of manoeuvrability of the fish is its ability to reorient through an angle, θ_f, in time, t_{θ_f}, whilst minimising its loss of kinetic energy (or maximising K'). A study of escapes in angelfish when startled by a lateral stimulus (Domenici & Blake 1993) indicated that fish escaped by turning through angles that varied between 30° and 120° from the initial swimming direction. Thus in this study we consider the time and the energy loss associated with a fish effecting a turn of 60°. Studies by Webb (1978) have shown that body depth has an important bearing on the manoeuvrability of fish. Thus we compare the depth dependence of the time, t_{60}, to turn through an angle, $\theta = 60°$, and the corresponding kinetic energy ratio, K'.

We use the numerical model (Model 2) and solve (3.22) to compute the response to a flexible bend given by expressions (4.5)–(4.7), with parameters, $h_o = 1$, $t_o = 1$, $s_o = l/2$. The body inertia distribution is given by $m_b = \pi/4d^2$. The variation with depth of t_{60} and K' are plotted in figure 7 for depths $0.2 \leqslant d \leqslant 1.0$. These comparisons show that t_{60} is a minimum at a depth of ~ 0.6. Conversely, K' decreases monotonically with depth. Thus a body depth of $d \sim 0.6$ generates the fastest turn for only an intermediate loss of energy.

To understand why there is an intermediate depth which generates the fastest turns, let us consider the principal factors that depend on body depth. The inertia of the fish increases as the square of the depth whilst the shed vorticity scales linearly with depth. Higher body inertia helps to accelerate the turn; conversely the shed wake has a dissipative contribution that inhibits the turn response and this wake-induced dissipation grows with time. Thus turning in slender fish ($d \sim 0.2$) is retarded due to reduced body inertia, whilst turning in deeper fish ($d \sim 1$) is inhibited by the shed wake dissipation effect. An intermediate depth of $d \sim 0.6$ balances these two contributions and generates the fastest turns. Since energy loss scales directly with rate of side-slip, which in turn depends on body inertia, the most slender fish benefit from the least loss in kinetic energy.

Furthermore, studies that model the internal muscle moments exerted by a flexible fish (Cheng *et al.* 1998) show that in order for the muscle contraction to be effective in generating a particular deflection, it must overcome the internal structural bending moment of the biological material itself, which in turn scales directly with depth.

https://doi.org/10.1017/jfm.2012.1 Published online by Cambridge University Press

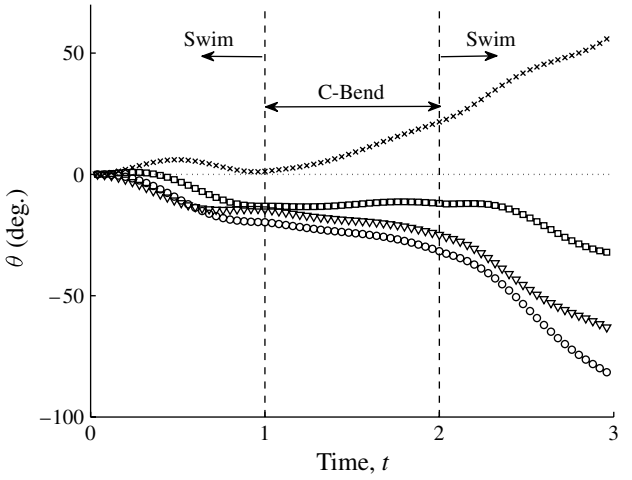


FIGURE 8. θ variation in time for the flexible bend performed for initial swimming with the manoeuvre commencing at different phases of swimming: $\varphi = 0$ (crosses), $\varphi = \pi/4$ (squares), $\varphi = \pi/2$ (circles), $\varphi = 3\pi/4$ (inverted triangles) where the phase lag, φ, is as defined for the swimming deflection function (5.7). (Body depth $d = 0.6$, see text in § 5.3 for the swimming and bend functions; the horizontal dotted line indicates the $\theta = 0$ axis.)

Computations (not shown here: Singh 2009) indicate that structural bending moments are significantly higher for angelfish (deeper bodies) compared to pike (slender bodies). Hence greater body depths suggest there is a larger penalty associated with the losses in kinetic energy as well as internal losses due to the structure. Although our computations suggest that the time to turn is comparable for fish of depths $0.5 < d < 1$, the energy loss that a fish must contend with grows rapidly with depth.

Finally, we note that the fish exercises its ability to control fin deflections and neural processes are likely to come into play to seek out the quickest or the most energetically efficient fin deployment strategy. The tools developed here are amenable to the development of optimal control strategies, but such a study is outside the scope of this particular work.

5.3. *Enhancing manoeuvrability by swimming*

In a study on the role of various turning gaits, Boyer *et al.* (2008) examined the effect of the duration of bending of the body on the angle of turn and they showed that the turn angle increased if the asymmetric bend was performed for a longer duration of time. In this section we consider more subtle aspects related to turning whilst swimming; these are the initial conditions of the swimmer prior to the bend and the possibility of energy extraction from the prior wake shed during swimming. The fish is modelled with the optimal depth, $d = 0.6$.

For swimming prior to the bend, in time interval $0 < t < 1$, the fish undergoes undulatory swimming as given by the function,

$$y(s, t) = (A - \mathrm{i}Bs)\mathrm{e}^{\mathrm{i}(ks-\omega t-\varphi)}, \tag{5.7}$$

where parameters are: $A = 0.05$, $B = 0.1$, $k = 1$, $\omega = 2\pi$. The importance of the phase-lag parameter, φ, is examined first. In the time interval, $1 < t < 2$, the fish executes a 'C-bend', after which time ($t > 2$) it resumes undulatory swimming in the new direction. All parameters associated with the C-bend are as prescribed in § 5.2.

https://doi.org/10.1017/jfm.2012.1 Published online by Cambridge University Press

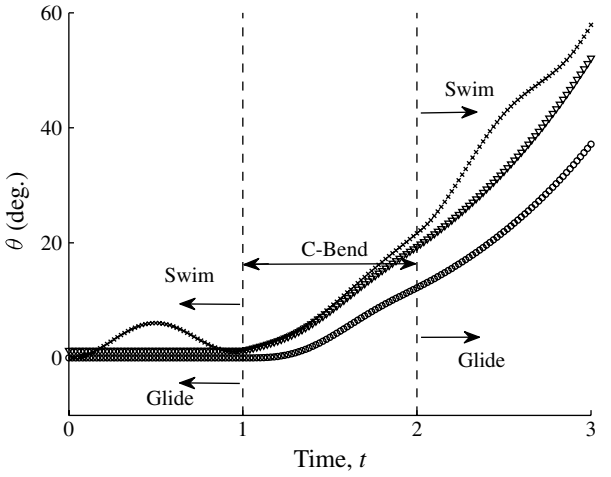


FIGURE 9. θ variation in time for a flexible bend performed for three cases: (*a*) an initial glide (circles), (*b*) an initial swimming condition (crosses), (*c*) a glide with swimming initial conditions (inverted triangles). (Body depth $d = 0.6$, see text in § 5.3 for the swimming and C-bend functions and initial conditions.)

In figure 8 we compare the turn response for four different values of phase lag, $\varphi = 0, \pi/4, \pi/2, 3\pi/4$. Since the rigid-body dynamic state of the fish varies over the undulatory swimming period, the turn response of the fish depends on at what phase of undulation the manoeuvre commences and we find that the magnitude and even the direction of the turn can change depending upon the phase of undulation. Although subtleties exist in the onset of manoeuvres, the most interesting outcome of this comparison is that through appropriate combinations of symmetric undulations and asymmetric bends the fish can change the magnitude as well as the sign of the turn angle, for the same body deflection.

Next we compare the effect of initial conditions and shed vorticity on enhancement of the turning response. Prior work on swimming and manoeuvring has suggested that fish manipulate previously shed vortices to enhance their manoeuvring capabilities (Wolfgang *et al.* 1999). The objective of this comparison is to understand whether it is the rigid-body dynamic state of the fish or energy extraction by prior shed wake vortices that is effective in enhancing the manoeuvrability. In figure 9 we compare the turn angle response in time for three initial conditions: (*a*) an initial glide; (*b*) an initial swim; and (*c*) an initial glide from which the bend is started with the same initial conditions as the swimming case. Thus in case (*a*) prior to the flexible bend ($t < 1$), the fish glides along $-\hat{\boldsymbol{i}}$ with speed, $U_o = 1$. In the interval, $1 < t < 2$, the fish executes a flexible bend, and for $t > 2$ it resumes gliding in the new direction. Case (*b*) is identical to the ($\varphi = 0$) configuration examined in figure 8. Case (*c*) is similar to case (*a*) except the rigid-body conditions at $t \leqslant 1$ are selected to be identical to those computed in case (*b*) at $t = 1$, hence in cases (*b*) and (*c*) at the initiation of the bend ($t = 1$) the fish possess the same initial $\theta, \dot{\theta}$ and $V_{x,o}, V_{y,o}$. Comparing the response for cases (*a*) and (*b*) we find that the turn-angle at the end of the bend ($t = 2$) is significantly larger when the fish is initially swimming. However, comparisons with (*c*) suggest rather small differences exist between (*b*) and (*c*) (at $t = 2$). The principal difference between cases (*b*) and (*c*) is that the vorticity shed for initial swimming (case *b*) is absent in case (*c*). These computations suggest that the

https://doi.org/10.1017/jfm.2012.1 Published online by Cambridge University Press

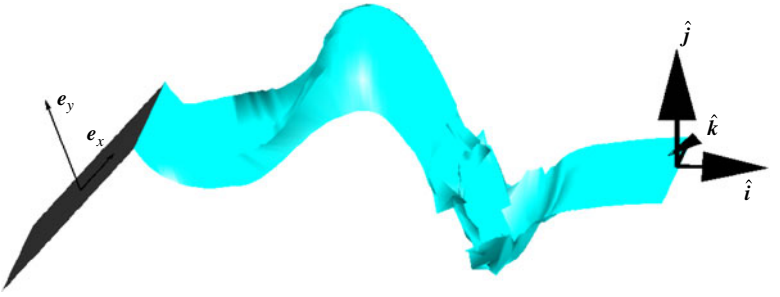


FIGURE 10. (Colour online available at journals.cambridge.org/flm) C-bend after a glide (at time $t = 2.3$ corresponding to case a in figure 9): three-dimensional snapshot of the fish (dark grey surface) and its wake (light grey surface, cyan online) evolving in time.

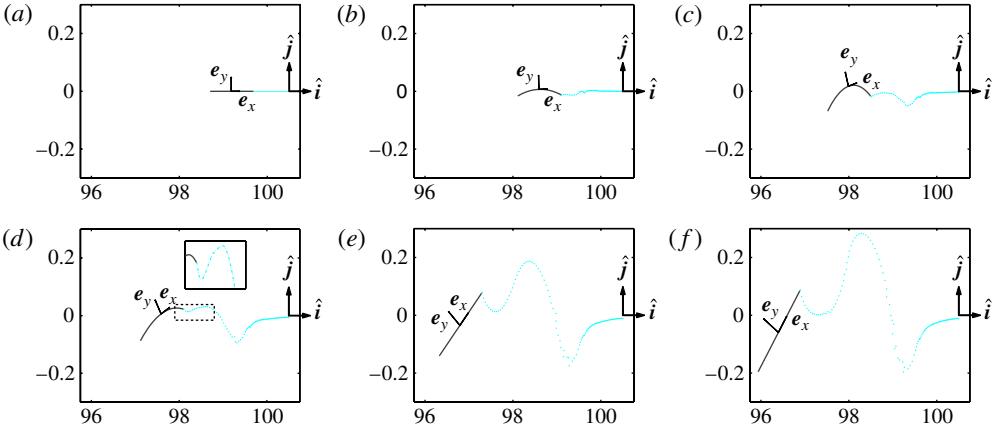


FIGURE 11. (Colour online) C-bend after a glide: two-dimensional section of the body (dark grey curve) and the evolving wake (light grey dots, cyan online) at different instants in time as the fish performs a flexible bend (also see three-dimensional snapshot of the fish in figure 10, to correlate times refer to figure 9). The enlarged view of the trailing edge at time $t = 1.7$ (inset in d) shows the wake vortex section (indicated by dashed lines) shed tangential to the body: (a) $t = 0.80$; (b) $t = 1.20$; (c) $t = 1.50$; (d) $t = 1.70$; (e) $t = 2.10$; (f) $t = 2.30$.

dominant contribution to turning comes about from the initial rigid-body dynamic state of the fish just prior to the bend, rather than by extracting energy from the wake.

To visually examine the process of self-propelled manoeuvring and vortex shedding, in figures 10–13 we plot snapshots in time of the fish turning after an initial glide and turning after initially swimming ($\varphi = 0$). Figures 10 and 12 show three-dimensional views for the glide-bend (case a) and swim-bend (case b) compared in figure 9. The views of the two-dimensional mid-span section at different instants of time indicating the progression of the fish and the evolution of the wake vorticity can be compared in figures 11 and 13. Note that the wake vorticity surface when shed is tangential to the body in accordance with the Kutta condition and the enlarged view near the trailing edge in the inset of figure 11(d) ($t = 1.7$) confirms the tangential nature of the shed wake. The computations show that the shed wake evolves as the body manoeuvres and, as the bend grows in magnitude, the higher body-bound vorticity induces larger wake

https://doi.org/10.1017/jfm.2012.1 Published online by Cambridge University Press

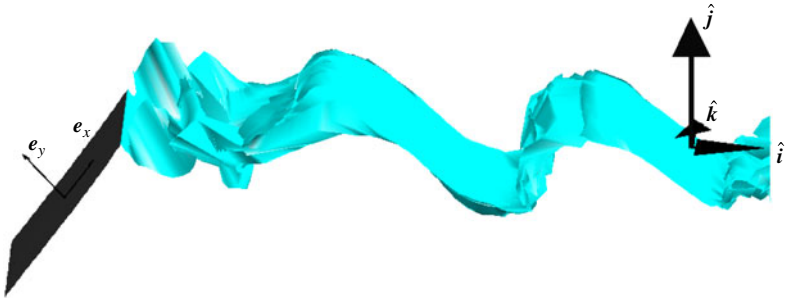


FIGURE 12. (Colour online) C-bend after undulatory swimming (at time $t = 2.3$ corresponding to case *b* in figure 9): three-dimensional snapshot of the fish (dark grey surface) and its wake (light grey surface, cyan online) evolving in time.

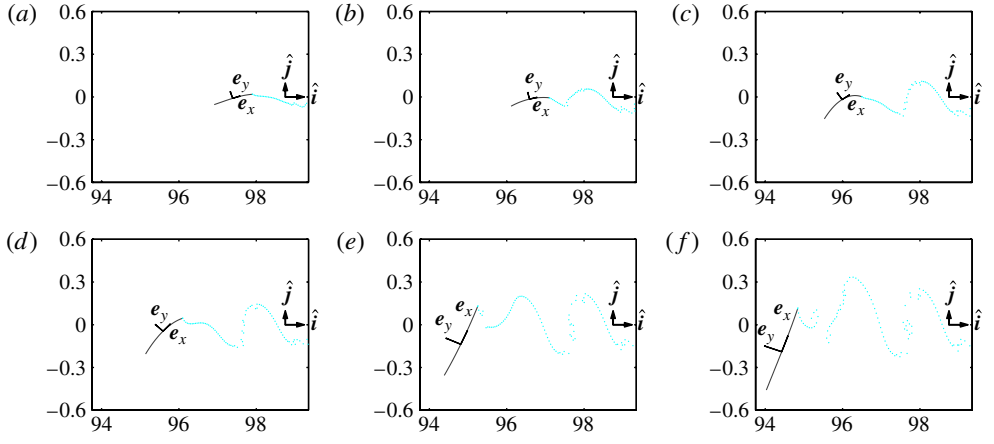


FIGURE 13. (Colour online) C-bend after undulatory swimming: two-dimensional section of the body (dark grey curve) and the evolving wake (light grey dots, cyan online) at different instants in time as the fish performs a flexible bend (see three-dimensional snapshot of the fish in figure 12, see figure 9 for times): (*a*) $t = 0.80$; (*b*) $t = 1.20$; (*c*) $t = 1.50$; (*d*) $t = 1.70$; (*e*) $t = 2.10$; (*f*) $t = 2.30$.

velocities causing the near wake to deform. For the undulatory swimming condition, the wake progressively deforms as a vortex pair which is shed during the initial undulatory swimming cycle. We see that qualitatively the wake vorticity during a turn is very similar to the initial glide case, although the wake vorticity strength is higher for the initially swimming configuration. Since the vortex-induced velocity scales as r^{-2}, the diminishing influence of the wake vorticity on the turn dynamics is consistent with the observed response in figure 9 as well as with the wake signature in figures 10–13. The advantage of modelling the fully coupled body-inertia fluid-dynamic system of equations is that we are in a position to confirm the importance of the initial dynamic state of the fish.

6. Conclusions

The main objective of this work is to apply insights from studies on forward propulsion of fish or fish-like swimmers in order to examine more general locomotion

https://doi.org/10.1017/jfm.2012.1 Published online by Cambridge University Press

and thereby model conditions that a typical fish would be subjected to. We use the approach developed by Cheng *et al.* (1991) and Hill (1998) as the foundation. The fish is modelled using a boundary-element method based on a system of elemental rectangular vortex rings, which effectively corresponds to a hydrodynamic model of an infinitely thin swimmer (Model 2). Momentum conservation on the body is enforced in order to solve for the body-inertia–fluid-dynamic interaction. As a consequence, the rigid-body motion or recoil correction is determined.

To verify the numerical model we use the approach of Kambe (1978), who extended the elongated-body theory of Lighthill (1960) and applied a correction for wake shedding proposed by Wu (1971*b*) to study the rigid-body response to an impulsive manoeuvre. In Model 1 we extend Kambe's approach to include flexible body motion; the observed agreement in turning response with Model 2 is interpreted as validation of both the models.

The numerical model is applied to analyse manoeuvrability in flexible swimmers. Based on observations of escape manoeuvres in nature we prescribe a flexible bend function to mimic observed 'C-bends' (Gray 1933). We employ this approach to examine the role of body depth on the turn dynamics. Computations for depths varying in the range $0.2 \leqslant d \leqslant 1.0$ suggests that an intermediate depth ($d \sim 0.6$) is optimal for rapid turns through large angles. A fish of intermediate depth appears to benefit from a higher body inertia, a lack thereof in a slender fish inhibiting its turn response. Conversely, deeper bodied fish are restrained by the dampening effect of the shed wake.

The numerical computations enable us to understand how a flexible-bodied swimmer might enhance its manoeuvrability by commencing a flexible bend at an appropriate period of undulatory swimming. Comparisons of bends between glide events and swimming events indicate that the fish principally uses its initial body dynamics to enhance its turn angle and to determine its sign; the wake vortices shed whilst swimming have a much weaker effect on enhancing the turn dynamics.

Observations from nature show that ray-finned fish extend and retract their fins, thereby dynamically changing their shape in the course of effecting a turn. Computations using Model 2 demonstrate that a rectangular fish of intermediate depth is optimally suited for rapid changes in swimming direction; conversely preliminary calculations from Model 1 suggest that an elliptical geometric shape is desirable from a stability point of view. These comparisons of shape dependence of manoeuvrability and stability suggest the advantage that a fin-like control surface introduces. A natural extension of this work is to include representative fish-like geometries in the numerical model, by including the wake shed from sharp-edged dorsal and ventral fins to examine the role of such shapes from a manoeuvrability perspective.

We have also neglected viscous effects of the fluid in these calculations. In modelling complex manoeuvres from rest the viscous contribution may become much more important. One approach would be to model these as resistive force components as proposed by Taylor (1952) and employed by McMillen & Holmes (2006) and Boyer *et al.* (2008). Finally, in this work we exclusively concentrate on the mechanical aspects of manoeuvres in fish; we have not accounted for biological aspects such as muscle action of the swimmer. We are currently pursuing this aspect following Wu (1971*a*), Cheng *et al.* (1998) and Pedley & Hill (1999).

https://doi.org/10.1017/jfm.2012.1 Published online by Cambridge University Press

Acknowledgements

The authors wish to acknowledge DAMTP, University of Cambridge and Fitzwilliam College for financial support of this work, and the anonymous referees for their valuable suggestions and feedback.

Appendix A. Solution algorithm

In § 2.2.2 we outlined the solution formulation. Here we present the algorithm (also refer to figure 1).

(*a*) At time instant t prescribe curve $\mathscr{C}$, constrained by the length-preserving criterion, (2.11). This establishes position vector $\boldsymbol{x}_1(s,t)$ of an arbitrary point on the body relative to reference point, P'.

(*b*) From (2.9) compute the position vector of the centre of mass, P, relative to P'.

(*c*) From (2.10) determine the position vector, $\boldsymbol{r}$, of all points on the body with respect to P.

(*d*) Determine the increment in position vector of the centre of mass, $\boldsymbol{R}_o(t)$, and orientation, $\theta(t)$, over the previous time step by solving equations of motion, (2.17)–(2.18), subject to initial conditions, (2.19) and (2.20). Update the inertial coordinates of each point on the body, $\boldsymbol{R}(s,t)$. Iterate this step until convergence is acquired within acceptable bounds.

(*e*) The algorithm proceeds to the next time step.

Appendix B. Definitions

Definitions of the coefficients used in (3.8), (3.9), (3.10) and (3.22):

$$a_{x,1}(t) = \int_0^l m_b(x\sin\theta + y\cos\theta)\,\mathrm{d}s, \tag{B 1a}$$

$$a_{x,2}(t) = 2\int_0^l m_b(\dot{x}\sin\theta + \dot{y}\cos\theta)\,\mathrm{d}s, \tag{B 1b}$$

$$a_{x,3}(t) = \int_0^l m_b(\ddot{x}\cos\theta - \ddot{y}\sin\theta - \dot{\theta}^2(x\cos\theta - y\sin\theta))\,\mathrm{d}s, \tag{B 1c}$$

$$a_{y,1}(t) = \int_0^l m_b(x\cos\theta - y\sin\theta)\,\mathrm{d}s, \tag{B 2a}$$

$$a_{y,2}(t) = 2\int_0^l m_b(\dot{x}\cos\theta - \dot{y}\sin\theta)\,\mathrm{d}s, \tag{B 2b}$$

$$a_{y,3}(t) = \int_0^l m_b(\ddot{x}\sin\theta + \ddot{y}\cos\theta - \dot{\theta}^2(x\sin\theta + y\cos\theta))\,\mathrm{d}s, \tag{B 2c}$$

$$a_{z,x}(t) = \int_0^l m_b(x\sin\theta + y\cos\theta)\,\mathrm{d}s, \tag{B 3a}$$

$$a_{z,y}(t) = \int_0^l m_b(x\cos\theta - y\sin\theta)\,\mathrm{d}s, \tag{B 3b}$$

$$a_{z,1}(t) = \int_0^l m_b(x^2 + y^2)\,\mathrm{d}s, \tag{B 3c}$$

https://doi.org/10.1017/jfm.2012.1 Published online by Cambridge University Press

$$a_{z,2}(t) = 2\int_0^l m_b\,(\dot{x}x + \dot{y}y)\;\mathrm{d}s, \tag{B 3d}$$

$$a_{z,3}(t) = \int_0^l m_b\,(-\ddot{x}y + \ddot{y}x)\;\mathrm{d}s. \tag{B 3e}$$

The expressions for the fluid-dynamic contribution in (3.10) are

$$a_i(t) = -\int_0^l \sin\chi\,\tilde{a}_i\,\mathrm{d}s \tag{B 4a}$$

$$b_i(t) = \int_0^l \cos\chi\,\tilde{a}_i\,\mathrm{d}s \tag{B 4b}$$

$$c_i(t) = \int_0^l (x\cos\psi + y\cos\psi)\tilde{a}_i\,\mathrm{d}s \tag{B 4c}$$

where subscript i varies from (0, 6) and corresponds to expressions,

$$\begin{aligned}\tilde{a}_0(s,t) = {} & m_a(\dot{\theta}(\dot{R}_y\sin\chi + \dot{R}_x\cos\chi) - (-\ddot{x}\sin\psi + \ddot{y}\cos\psi)\\ & - (\dot{\psi} + U\chi')(\dot{x}\cos\psi + \dot{y}\sin\psi) + U\dot{\psi})\\ & - m_a'U(1-\epsilon_1)(-\dot{x}\sin\chi + \dot{y}\cos\chi)\end{aligned} \tag{B 5a}$$

$$\tilde{a}_1(s,t) = m_a\cos\chi(\chi'U + \dot{\psi}) + m_a'(s)U(1-\epsilon_1)\sin\chi \tag{B 5b}$$

$$\tilde{a}_2(s,t) = m_a\sin\chi(\chi'U + \dot{\psi}) - m_a'(s)U(1-\epsilon_1)\cos\chi \tag{B 5c}$$

$$\begin{aligned}\tilde{a}_3(s,t) = {} & m_a(-(\dot{x}\cos\psi + \dot{y}\sin\psi) - (\dot{\psi} + U\chi')\\ & \times(-x\sin\psi + y\cos\psi) + U) - m_a'U(1-\epsilon_1)(x\cos\psi + y\sin\psi)\end{aligned} \tag{B 5d}$$

$$\tilde{a}_4(s,t) = m_a\sin\chi \tag{B 5e}$$

$$\tilde{a}_5(s,t) = -m_a\cos\chi \tag{B 5f}$$

$$\tilde{a}_6(s,t) = -m_a(x\cos\psi + y\sin\psi). \tag{B 5g}$$

$\psi(s,t) = \chi(s,t) - \theta(t)$ and is the tangent angle made by point s on $\mathscr{C}$ with respect to the body frame $\{\boldsymbol{e}_x, \boldsymbol{e}_y\}$.

Appendix C. Numerical convergence of Model 2

In §C.1 we examine the spatial convergence of the numerical scheme, the objective being to identify the optimal number of chordwise and spanwise points (N_x, N_z) in order that computational cost is balanced by accuracy in results. We employ the result of the temporal convergence study by Hill (1998), which leads to the choice of time step size: $\Delta t = \Delta x/U$. We discuss key aspects of this temporal convergence study in §C.2.

C.1. *Spatial discretisation*

The algorithm uses first-order integration along x and z. To check for first-order accuracy in x we maintain a constant number of spanwise points and vary the number of chordwise points. We apply the following deflection function to model flexible swimming:

$$y(s,t) = (A - \mathrm{i}B(s - s_o))\,\mathrm{e}^{\mathrm{i}(ks-\omega t)}. \tag{C 1}$$

For the convergence tests we choose $A = 0.005, B = 0.012, s_o = 0, \omega = 2\pi, k = 3$ for a depth of $d = 0.1$, chosen to account for the three-dimensional fluid-dynamic effects.

https://doi.org/10.1017/jfm.2012.1 Published online by Cambridge University Press

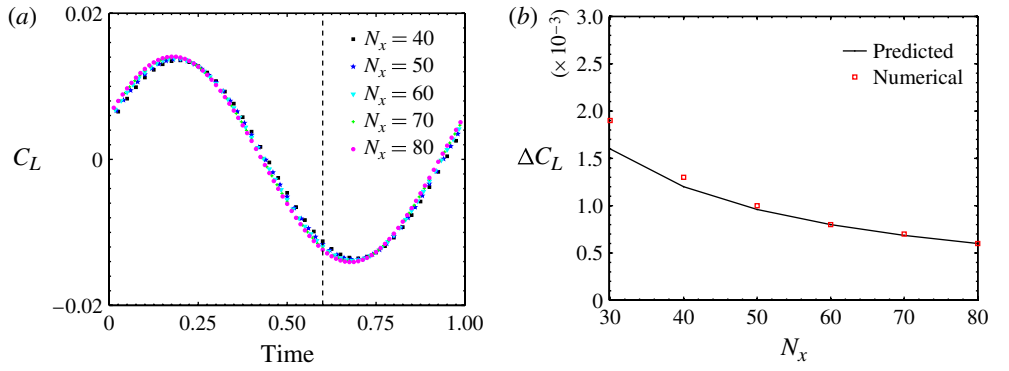


FIGURE 14. (Colour online) Side force coefficient, C_L, variation for increasing number of chordwise points for a swimmer performing undulatory oscillations corresponding to (C 1) with frequency $\omega = 2\pi$, wavenumber $k = 3$, spanwise points $N_z = 5$ (as stated in the text $A = 0.005, B = 0.012, s_o = 0, d = 0.1$). (*a*) Variation of C_L with time for increasing number of chordwise points. (*b*) Comparison of the prediction from (C 2) of ΔC_L with the numerical values for increasing number of chordwise points.

For variation in the number of discrete elements N_x, N_z, the time-varying response of the side force C_L and yaw moment C_M was similar, hence we choose C_L to examine the convergence. In figure 14(*a*) we plot the C_L variation in time for N_x varying from 30 to 80 and $N_z = 5$, and observe that the solutions converge to a consistent value at high values of N_x. We examine the accuracy of the numerical scheme in figure 14(*b*) by comparing the ΔC_L variation with the predicted value from the first term in the Taylor series expansion. The increment in lift at the current time t_i is given by

$$\Delta C_L(t_i) = C_L(t_i) - C_L(t_{i-1}) = \left(\frac{\partial C_L}{\partial t}\right)_{t_{i-1}} \Delta t, \\ = \left(\frac{\partial C_L}{\partial t}\right)_{t_{i-1}} \frac{1}{N_x}; \tag{C 2}$$

when $U = 1$ we have $\Delta t = \Delta x/U = 1/N_x$. Thus the numerical value of $\Delta C_L(t_i)$ is expected to scale as $1/N_x$ if the numerical integration is correctly implemented and the physical phenomena are correctly captured at small enough N_x. Choosing the value for $(\partial C_L/\partial t)_{t_{i-1}}$ at $N_x = 80$, in figure 14(*b*) we plot the values at time $t = 0.6$ (the instant when the differences between the computations are the greatest). We see that $1/N_x$ behaviour is observed for values of $N_x \geqslant 50$ with an error of less than 2.5 %. To balance computational cost with accuracy we select $N_x = 50$ for all our simulations.

In figure 15 we compare the time-varying response of C_L for varying number of spanwise points N_z. The kinematic parameters are the same as above; we have set $N_x = 50$ and N_z is varied from 5 to 20. The variation in response drops off for rather low values of N_z. We analyse the results for a rectangular plate of small depth, $(d = 0.1)$, to ensure that the dependence on spanwise terms is captured. The variation in C_L with spanwise elements is small, suggesting that the pressure is principally dependent on the chordwise components of the flow. For high-aspect-ratio plates we observe virtually no difference in results for increasing N_z and the value of $N_z = 5$ is more than adequate to capture the relevant behaviour. Based on the results in this study, for the model of fish with small depths $(d < 0.25)$ we choose $N_x = 50, N_z = 10$;

https://doi.org/10.1017/jfm.2012.1 Published online by Cambridge University Press

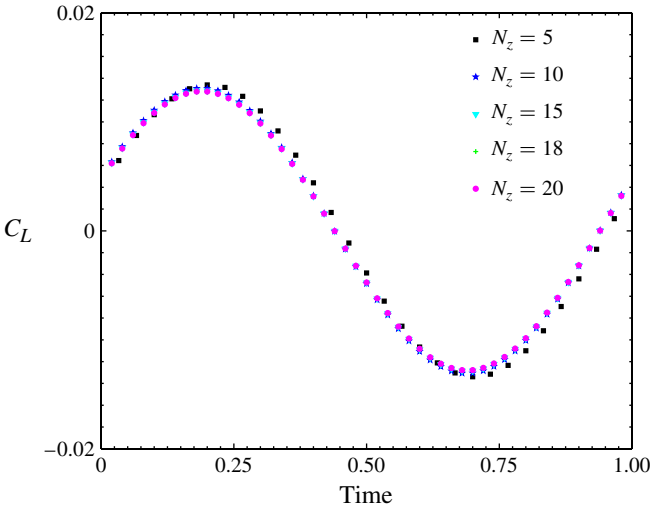


FIGURE 15. (Colour online) Lift coefficient, C_L, variation with spanwise elements for a swimmer performing undulatory oscillations at frequency $\omega = 2\pi$, wavenumber $k = 3$, $N_x = 50$ (as stated in the text $A = 0.005$, $B = 0.012$, $s_o = 0$, $d = 0.1$).

for fish of larger depths ($d > 0.25$) we choose $N_x = 50$, $N_z = 5$, and $\Delta t = \Delta x/U$ for all cases.

C.2. *Temporal discretisation*

Our choice of temporal discretisation, $\Delta t = \Delta x/U$, is based on the study by Hill (1998) on temporal convergence for a two-dimensional point-vortex-based undulatory swimmer. Note that we have compared the fluid-dynamic forces for a two-dimensional point vortex method with the three-dimensional vortex ring method for a large-aspect-ratio flexible plate and the agreement in results suggests Hill's results from the temporal convergence analysis may be applied to both models. Here we summarise and briefly discuss the results of Hill's study.

For swimming deflection function (C 1) with parameters $A = 0.05, B = 0.12$ and $\omega = 2\pi, k = 1$ and 7, flow speed $U = 1$, the pressure difference $\Delta p(x, t)$ in an oscillation period was compared for different time steps. Hill fixed the chordwise element size ($\Delta x = 0.02$) and varied time step Δt (from $0.01, 0.02, 0.03, 0.05$) and demonstrated that the pressure difference near the trailing edge is strongly affected by the choice of Δt. It was noted that for $\Delta t = \Delta x$, the trailing-edge pressure difference is a minimum. Recall that at the trailing edge ($x = 1$) the steady Kutta condition requires $\Delta p = 0$. In the numerical model the trailing collocation point, where the boundary conditions are applied and pressure is computed, is a distance $\Delta x/4$ ahead of the trailing edge. Conversely, the shed vortex point (or line element) is $\Delta x/4$ behind the trailing edge and as Δx decreases the pressure difference at the trailing element approaches zero. As the body moves along $-\boldsymbol{e}_x$, in $U\Delta t$ spatial steps, the vortex ring definition sets the spacing between consecutive wake vortex rings and the most recently shed wake vortex. The spacing between consecutive wake vortex rings is $U\Delta t$ and as this spacing differs from Δx, the influence on the body-bound vorticity varies. Note from (3.13) that the velocity induced by the vortex scales as $1/r^2$, correspondingly this variation in spacing between the wake vortices has its strongest

https://doi.org/10.1017/jfm.2012.1 Published online by Cambridge University Press

influence on the trailing element and thereby the pressure difference near the trailing edge is primarily affected. In choosing $\Delta t = \Delta x$, we see that the upstream effect of previously shed wake vorticity will not violate the Kutta condition.

It is important to note that the above-mentioned influence of the position of the wake vortex only explains its contribution to the steady term in the expression for the pressure difference. As the motion becomes increasingly unsteady, the added mass term in Δp becomes significant, causing the pressure difference to become non-zero at the trailing edge. To correct this error would require an extra step in the algorithm to reset the position and orientation of the shed wake at the trailing edge. Although Basu & Hancock (1978) developed an approach for a two-dimensional unsteady aerofoil, as yet we have not employed this approach or developed it for the vortex ring method; at present we monitor the pressure difference to ensure the error is bounded below 5 % of peak pressure difference.

REFERENCES

BASU, B. C. & HANCOCK, G. J. 1978 The unsteady motion of a two-dimensional aerofoil in incompressible inviscid flow. *J. Fluid Mech.* **87**, 159–178.

BATCHELOR, G. K. 1967 *An Introduction to Fluid Dynamics*. Cambridge University Press.

BOYER, F., POREZ, M. & LEROYER, A. 2010 Poincaré-Cosserat equations for the Lighthill three-dimensional large amplitude elongated body theory: application to robotics. *J. Nonlinear Sci.* **20**, 47–79.

BOYER, F., POREZ, M., LEROYER, A. & VISONNEAU, M. 2008 Fast dynamics of an eel-like robot: Comparisons with Navier–Stokes simulations. *IEEE Trans. Robot.* **24**, 1274–1288.

CHENG, J. Y., PEDLEY, T. J. & ALTRINGHAM, J. D. 1998 A continuous dynamic beam model for swimming fish. *Phil. Trans. R. Soc. Lond.* B **353**, 981–997.

CHENG, J. Y., ZHUANG, L. X. & TONG, B. G. 1991 Analysis of swimming three-dimensional waving plates. *J. Fluid Mech.* **232**, 341–355.

DOMENICI, P. & BLAKE, R. W. 1993 Escape trajectories in angelfish (Pterophyllum Eimekei). *J. Expl Biol.* **177**, 253–272.

DOMENICI, P. & BLAKE, R. W. 1997 The kinematics and performance of fish fast-start swimming. *J. Expl Biol.* **200**, 1165–1178.

DRUCKER, E. G. & LAUDER, G. V. 2001 Wake dynamics and fluid forces of turning maneuvers in sunfish. *J. Expl Biol.* **204**, 431–442.

ETKIN, B. & REID, L. D. 1996 *Dynamics of Flight, Stability and Control*. Wiley.

GRAY, J. 1933 Directional control of fish movement. *Proc. R. Soc. Lond.* B **113** (770), 115–125.

HILL, S. J. 1998 Large amplitude fish swimming. PhD thesis, University of Leeds, Department of Applied Mathematics.

KAMBE, T. 1978 The dynamics of carangiform swimming motions. *J. Fluid Mech.* **87**, 533–560.

KANSO, E. 2009 Swimming due to transverse shape deformations. *J. Fluid Mech.* **631**, 127–148.

KATZ, J. & PLOTKIN, A. 2001 *Low Speed Aerodynamics*, 2nd edn. Cambridge University Press.

KRASNY, R 1986 Desingularisation of periodic vortex sheet roll-up. *J. Comput. Phys.* **65**, 292–313.

LAN, C. E. 1979 The unsteady quasi-vortex-lattice method with applications to animal propulsion. *J. Fluid Mech.* **93**, 747–765.

LIGHTHILL, M. J. 1960 Note on the swimming of slender fish. *J. Fluid Mech.* **9**, 305–317.

LIGHTHILL, M. J. 1971 Large-amplitude elongated-body theory of fish locomotion. *Proc. R. Soc. Lond.* **179**, 125–138.

LIGHTHILL, M. J. 1977 Mathematical theories of fish swimming. In *Fisheries Mathematics* (ed. J. H. Steele), pp. 131–144. Academic.

MCCUTCHEN, C. W. 1976 Flow visualization with stereo shadowgraphs of stratified fluid. *J. Expl Biol.* **65** (1), 11–20.

MCMILLEN, T. & HOLMES, P. 2006 An elastic rod model for anguilliform swimming. *J. Math. Biol.* **53**, 843–866.

https://doi.org/10.1017/jfm.2012.1 Published online by Cambridge University Press

McMillen, T., Williams, T. L. & Holmes, P. 2008 Nonlinear muscles, passive viscoelasticity and body taper conspire to create neuro-mechanical phase lags in anguilliform swimmers. *PLoS Comp. Biol.* **4** (8), doi:10.1371/ journal.pcbi.1000157.

Pedley, T. J. & Hill, S. J. 1999 Large-amplitude undulatory fish swimming: fluid mechanics coupled to internal mechanics. *J. Expl Biol.* **202**, 3431–3438.

Press, W. H., Teukolsky, S. A, Vetterling, W. T. & Flannery, B. P. 2007 *Numerical Recipes: The Art of Scientific Computing*, 3rd edn. Cambridge University Press.

Robinson, A & Laurmann, J. A. 1956 *Wing Theory*. Cambridge University Press.

Singh, K. 2009 Hydrodynamics of flexible manoeuvres in fish. PhD thesis, University of Cambridge, Department of Applied Mathematics and Theoretical Physics.

Taylor, G. I. 1952 Analysis of the swimming of long and narrow animals. *Proc. R. Soc. Lond.* A 158–183.

Videler, J. J. & Hess, F. 1984 Fast continuous swimming of pelagic predators, saithe (Pollachius virens) and mackeral (Scomber scombrus): a kinematic analysis. *J. Expl Biol.* **109**, 209–228.

Webb, P. W. 1978 Fast-start performance and body form in seven species of teleost fish. *J. Expl Biol.* **74**, 211–226.

Weihs, D. 1972 Hydrodynamic analysis of fish turning manoeuvres. *Proc. R. Soc. Lond.* **182**, 59–72.

Wolfgang, M. J., Anderson, J. M., Grosenbaugh, M. A., Yue, D. K. P. & Triantafyllou, M. S. 1999 Near-body flow dynamics in swimming fish. *J. Expl Biol.* **202**, 2303–2327.

Wu, T. Y. T. 1961 Swimming of a waving plate. *J. Fluid Mech.* **10**, 321–344.

Wu, T. Y. T. 1971*a* Hydromechanics of swimming propulsion. Part1. Swimming of a two dimensional flexible flat plate at variable forward speed in an inviscid fluid. *J. Fluid Mech.* **46**, 337–355.

Wu, T. Y. T. 1971*b* Hydromechanics of swimming propulsion. Part 3. Swimming and optimum movements of slender fish with side fins. *J. Fluid Mech.* **46**, 545–568.

Wu, T. Y. T 1977 Introduction to the scaling of aquatic animal locomotion. In *Scale Effects in Animal Locomotion* (ed. T. J. Pedley), pp. 203–232. Academic.

Wu, T. Y. 2011 Fish swimming and bird/insect flight. *Annu. Rev. Fluid. Mech.* **43**, 25–58.

https://doi.org/10.1017/jfm.2012.1 Published online by Cambridge University Press